

GEOMETRIC STRUCTURE AND DESORPTION KINETICS OF CO ON THE
 $\text{Cr}_2\text{O}_3(0001)/\text{Cr}(110)$ SURFACE

THESIS

Presented to the Graduate Council of
Texas State University – San Marcos
in Partial Fulfillment
of the Requirements

for the Degree

Master of SCIENCE

by

Gabriel Arellano, B.S.

San Marcos, Texas
May 2010

GEOMETRIC STRUCTURE AND DESORPTION KINETICS OF CO ON THE
Cr₂O₃(0001)/Cr(110) SURFACE

Committees Members Approved:

Carl A. Ventrice, Jr., Chair

Nikoleta Theodoropoulou

Wilhelmus J. Geerts

Approved:

J. Michael Willoughby
Dean of the Graduate College

COPYRIGHT

by

Gabriel Arellano

2010

ACKNOWLEDGEMENTS

I am indebted to Dr. Carl A Ventrice Jr. for his dedication as a mentor throughout my research, as an instructor here at Texas State University-San Marcos and for his patience and inviting manner of imparting his knowledge on the subject of Physics and everyday mechanics. Dr. Ventrice revitalized my interest in Physics by making the subject interesting, sensibly applicable and approachable and by never dismissing my questions or understanding about the subject. My loving appreciation is also extended to my friends and classmates here at Texas State; Nick Clark, Chris Cumby, Dan Fields, Greg Hodges, Rob Kilbourn, Chris Lohn, Nick Miller, Dan Ralls, Simona Rieman, Jennifer Walters, Jason Williams and Craig and to my friends and classmates at the University of Texas at Austin; Jay Palermo, Arturo Perez, Yingyue Li Boretz and Maia. Their humor, consideration and persistence were my therapy and motivation throughout my scholastic endeavors. To my best friends; Cesar R. Favela, Humberto E. Rodriguez, Richard Coronado, Felipe S. Ulloa, Tommy Murillo and Jason Williams; I thank you for pulling me out of my studies and helping me relax and for reminding me of the truly important qualities of life. I can never fully thank my mother, Chela Arellano, and my father, Lalo Arellano, for happily and unquestionably devoting so much of their life, their love and their guidance in raising me. I hope that they are as proud of me as their child as I am of them as my parents. To my brothers and sisters; Mickey, Magali, Becky, Rafael and Lupe, I thank you for always loving and accepting me for who I am and for who I want to be, but mostly for the humbling manner in which you sincerely show your

love and pride for me and for each other. To my beautiful wife, Lindsay Scott Rose-Arellano, I thank God for you, for you have shared all the hardships and blessings that have come with loving me as a husband and as a father with unwavering patience, attentiveness and with an unfathomable sense of humor. Finally, to my beautiful daughter Amalia Isabel Arellano, I thank you because, through you, I get to see the beauty of this world and reflect on the wonders of life and because you have made me a happier and better person.

TABLE OF CONTENTS

ACKNOWLEDGEMENTS	iv
LIST OF FIGURES	viii
LIST OF TABLES	x
ABSTRACT.....	xi
CHAPTER	
I. INTRODUCTION	1
II. CRYSTAL LATTICES AND ELECTRON DIFFRACTION.....	5
A. OVERVIEW OF CRYSTAL STRUCTURE	5
B. THE Cr(110) SURFACE	6
C. THE Cr ₂ O ₃ (0001) SURFACE	8
D. ELECTRON DIFFRACTION FROM A CRYSTAL SURFACE.....	10
E. CONSTRUCTING THE RECIPROCAL LATTICE OF Cr(110).....	18
III. EXPERIMENTAL TECHNIQUE.....	20
A. ULTRA HIGH VACUUM	20
B. VACUUM TECHNIQUES.....	24
C. LOW ENERGY ELECTRON DIFFRACTION OPTICS	28
D. CRYSTAL SAMPLE HOLDER	30
E. TEMPERATURE-PROGRAMMED DESORPTION	33
F. ANALYSIS OF ACTIVATION ENERGY USING TPD ANALYSIS	36
IV. EXPERIMENTAL RESULTS	39
A. PREPARATION OF THE Cr(110) SURFACE	39

B. GROWTH OF EPITAXIAL Cr ₂ O ₃ (0001) ON Cr(110)	43
C. TEMPERATURE DEPENDENT LEED ANALYSES OF Cr ₂ O ₃ (0001)/Cr(110).....	45
D. ADSORPTION OF CARBON MONOXIDE ON Cr ₂ O ₃ (0001)/Cr(110)..	47
i. CO DOSING SEQUENCE.....	47
ii. DEPENDENCE OF TPD SPECTRA ON HEATING RATE.....	51
iii. ACTIVATION ENERGY ANALYSIS	54
V. DISCUSSION	57
VI. CONCLUSIONS	61
REFERENCES	63

LIST OF FIGURES

Figure	Page
2-1. Five Bravais Lattices for 2-dimensional surface structures.....	6
2-2. Schematic of Chromium (Cr).....	7
2-3. Schematic of Cr ₂ O ₃ (0001) crystal.....	9
2-4. Plane wave incident on a spherical scattering center.....	11
2-5. Electron plane wave scattering from two electrons.....	13
2-6. Coordinate system and position vectors of electron cloud and j th atom.....	15
2-7. Theoretical real lattice drawing of Cr(110).....	18
2-8. Theoretical Reciprocal Lattice Drawing of Cr(110) based on the Laue condition.....	18
2-9. Observed LEED image of Cr(110) at room temperature with overlaid theoretical reciprocal lattice of Cr(110).....	19
3-1. Ultra-High Vacuum chamber with pumping system labeled.....	26
3-2. Ultra-High Vacuum chamber with mass spectrometer and x, y, z manipulator....	27
3-3. Schematic of electron gun and detector of LEED.....	29
3-4. Interior view of ultra-high vacuum chamber.....	31
3-5. x,y,z manipulator and ultra-high vacuum chamber viewport housing Cr(110) sample.....	32
3-6. Schematic of a quadrupole mass spectrometer (QMS).....	34
4-1. LEED analysis of Cr(110) after several sputter/anneal cycles at room temperature.....	42

4-2.	LEED analysis of Cr ₂ O ₃ (0001)/Cr(110) for this study	44
4-3.	LEED analysis of Cr ₂ O ₃ (0001)/Cr(110) at 300 K, 150 K and 90 K from a previous study	45
4-4	LEED analysis of Cr ₂ O ₃ (0001)/Cr(110) at ~ 300 K and 125 K for this study	46
4-5.	TPD spectra of CO from Cr ₂ O ₃ (0001)/Cr(110) at a heating rate of 10 °C/min for several doses of CO	49
4-6.	LEED analysis of CO/Cr ₂ O ₃ (0001)/Cr(110) for doses of 1 L and 10 L.....	50
4-7.	Pressure versus temperature curves for several heating rates for a CO dose of 1.0 L	53
4-8.	Arrhenius plot assuming first order desorption kinetics for a dose of 1.0 L of CO.....	56

LIST OF TABLES

Table		Page
4-1.	Areas calculated from pressure versus time curve and corresponding temperature of the maximum of the TPD peak.....	50
4-2	Areas calculated from pressure versus time curve and the temperature of the maximum of the TPD peak for heating rates ranging from 5 °C/min to 50 °C/min for a dose of 1.0 L of CO	54
4-3	Temperature of the maximum of the TPD peak for each dose of 1.0 L of CO	55

ABSTRACT

GEOMETRIC STRUCTURE AND DESORPTION KINETICS OF CO ON THE Cr₂O₃(0001)/Cr(110) SURFACE

by

Gabriel Arellano, B.S.

Texas State University – San Marcos

May 2010

SUPERVISING PROFESSOR: CARL A. VENTRICE Jr.

Understanding the interaction of simple molecules such as carbon monoxide on metal oxide surfaces is important for many industrial applications. For instance, Cr₂O₃ is an industrial catalyst used for the reduction on nitrogen oxide compounds and for the polymerization of various hydrocarbons. Previous groups have studied the adsorption of CO on the Cr₂O₃(0001)/Cr(110) surface and found that it lies flat on the surface instead of an upright geometry, which is observed on most other metal and metal oxide surfaces. In addition, there is only one published measurement of the activation energy for desorption of CO from Cr₂O₃(0001), and this value is approximately twice as high as the value calculated using quantum chemical cluster theory.

To determine the geometric structure of the clean and CO covered $\text{Cr}_2\text{O}_3(0001)/\text{Cr}(110)$ surface, we have performed temperature dependent low energy electron diffraction measurements of these surfaces. Our diffraction measurements reveal an unreconstructed clean $\text{Cr}_2\text{O}_3(0001)/\text{Cr}(110)$ surface over a temperature range of room temperature to 120 K. The diffraction pattern of the surface at a saturation coverage of CO shows only a slight increase in diffuse background with no overlayer reconstruction being observed. This is consistent with previous reports that CO molecules are easily desorbed by low energy electrons.

To determine the desorption kinetics of CO from the $\text{Cr}_2\text{O}_3(0001)/\text{Cr}(110)$ surface, we have performed temperature programmed desorption measurements. At a crystal temperature of 120 K, it was found that a saturation coverage of CO was obtained for a CO dose of ~ 1 L. The maximum of the desorption curve was observed to shift to higher temperature by only 4 K as the coverage approached saturation, which indicates a 1st order kinetics with an attractive adsorbate-adsorbate interaction. The activation energy for CO desorption was measured to be 49.2 ± 2.6 kJ/mol using the Redhead method with heating rates ranging from 5 °C/min to 50 °C/min.

CHAPTER I

INTRODUCTION

Chromium oxides are used in many industrial applications such as catalysts for polymerization and hydrocarbon reformation reactions, passivation of stainless steels, binder layers in magnetic media, and the active region of some gas sensors. To obtain a fundamental understanding of the surface properties of chromium oxide, it is beneficial to study the geometry and the desorption kinetics of simple molecules on the surfaces of this transition metal oxide.

Most industrial catalysts are used in powder form to increase the available surface area of the catalyst. Because of this, it is difficult to relate the interaction of the reacting molecules with a particular surface site since there will be several different terminations and a high defect density for a powdered material. To get a better understanding of the atomic scale interactions at the surface of a transition metal oxide, it is preferable to study adsorption on well-ordered surfaces of single crystals. Since insulating metal oxide crystals are ionic, the surfaces that are the most stable will be the non-polar surfaces, which are the surfaces with no net dipole moment normal to the surface. For Cr_2O_3 , the two primary non-polar surface terminations are (0001) and $(01\bar{1}2)$. Since most transition metal oxides are insulating, it becomes difficult to perform surface studies using electrons because of sample charging effects. One method of circumventing this problem is to study a thin film of the transition metal oxide on a metal substrate, which

allows excess charge to tunnel into the substrate. Since Cr_2O_3 grows epitaxially on the Cr(110) surface with a (0001) termination, this provides an excellent template for surface science studies of molecular adsorption.

The geometric structure of the clean $\text{Cr}_2\text{O}_3(0001)/\text{Cr}(110)$ surface has been studied using various surface sensitive experimental techniques.³⁻¹¹ An interesting property of this surface that was observed by previous groups using low energy electron diffraction (LEED) is the presence of a weak $(\sqrt{3}\times\sqrt{3})\text{R}30^\circ$ reconstruction at room temperature that becomes more distinct below $\sim 200\text{ K}$ and disappears below $\sim 100\text{ K}$.^{1,2} This reconstruction was observed to be reversible and was attributed to a surface magnetic transition. However, a recent temperature dependent LEED study of the $\text{Cr}_2\text{O}_3(0001)/\text{Cr}(110)$ surface did not observe the $(\sqrt{3}\times\sqrt{3})\text{R}30^\circ$ reconstruction at any temperature down to $\sim 120\text{ K}$.¹² Since CO adsorption on the $\text{Cr}_2\text{O}_3(0001)/\text{Cr}(110)$ surface results in a $(\sqrt{3}\times\sqrt{3})\text{R}30^\circ$ overlayer structure, it was proposed by Redding that the higher background chamber pressure of the previous studies may have resulted in CO adsorption on the surface instead of a surface reconstruction of the clean $\text{Cr}_2\text{O}_3(0001)$ surface.

There have been several studies of the adsorption of CO on the $\text{Cr}_2\text{O}_3(0001)/\text{Cr}(110)$ surface using a variety of surface sensitive experimental techniques.¹³⁻²⁰ As mentioned previously, CO is observed to form a $(\sqrt{3}\times\sqrt{3})\text{R}30^\circ$ overlayer structure at saturation coverage of a monolayer.² Since the CO layer is easily desorbed by low energy electrons, the LEED pattern of the CO is observed to disappear within about 10 s. For most single crystal surfaces, CO is observed to adsorb in a standing up configuration, usually with the C end of the molecule bonding to the surface. However, angle-resolved ultra-violet photoelectron spectroscopy (ARUPS)

measurements of CO on Cr₂O₃(0001)/Cr(110) have provided evidence for an unusual lying-down geometry.² Because of the sensitivity of the CO layer to secondary electrons, these measurements were performed in a background pressure of 7.5×10^{-6} Torr of CO. One of the issues regarding the adsorption of CO on Cr₂O₃(0001) that has not been fully resolved is the activation energy for desorption. A previous study of this system using quantum chemical cluster calculations has predicted an activation energy of 28 kJ/mol; whereas, thermal desorption spectroscopy (TDS) measurements resulted in an estimated activation energy of 45 kJ/mol.²⁰

In this thesis project, we have measured the temperature dependent surface structure of the clean Cr₂O₃(0001)/Cr(110) surface with LEED and also found no $(\sqrt{3} \times \sqrt{3})$ R30° reconstruction at temperatures down to 120 K. In addition, we have performed LEED measurements of the CO covered Cr₂O₃(0001) surface and have only observed a slight increase in diffuse background with no overlayer reconstruction, which is consistent with desorption of the CO due to the incident electron beam. Therefore, we conclude that there must be another mechanism for the observed temperature dependent $(\sqrt{3} \times \sqrt{3})$ R30° reconstruction by other groups. The most probable cause for this discrepancy is the much larger terrace step widths of our crystal since the surface alignment is 0.1° compared to 0.5° for the previously published results.¹

To determine the desorption kinetics of CO from the Cr₂O₃(0001)/Cr(110) surface, we have performed temperature programmed desorption (TPD) measurements. Only a slight change in the temperature of the desorption peak maximum is observed as the overlayer coverage is increased. This is consistent with a 1st order desorption kinetics and provides evidence that the CO is adsorbing molecularly (*i.e.*, the CO does not

dissociate into atomic C and O on the $\text{Cr}_2\text{O}_3(0001)$ surface). An activation energy for desorption has been measured using the Redhead method and results in a value of 49.2 ± 2.6 kJ/mol.

CHAPTER II

CRYSTAL LATTICES AND ELECTRON DIFFRACTION

A. OVERVIEW OF CRYSTAL STRUCTURE

A 3-dimensional crystal lattice is defined by a regular array of points in space, where each lattice point has the same translational symmetry.²⁵ The positions of the lattice points are defined by three translation vectors **a**, **b** and **c**. Therefore, a translation vector can be defined as

$$\mathbf{T} = n_1 \mathbf{a} + n_2 \mathbf{b} + n_3 \mathbf{c}, \quad [2-1]$$

where n_1 , n_2 , and n_3 are integers. This resulting structural array constitutes a crystal lattice. The translation vectors **a**, **b** and **c** construct a primitive cell and enclose the smallest volume defined as $\mathbf{a} \cdot (\mathbf{b} \times \mathbf{c})$.²⁵ A surface is 2-dimensional and is normally defined only by the position vectors **a** and **b**. When a surface is formed, the crystal loses its perfect translational symmetry perpendicular to the surface. Therefore, the surfaces of crystals always form two-dimensional lattices, known as nets.²⁶ There are five types of two-dimensional Bravais lattices: square, primitive rectangular, centered rectangular, hexagonal, and oblique, as shown below in Figure 2-1.

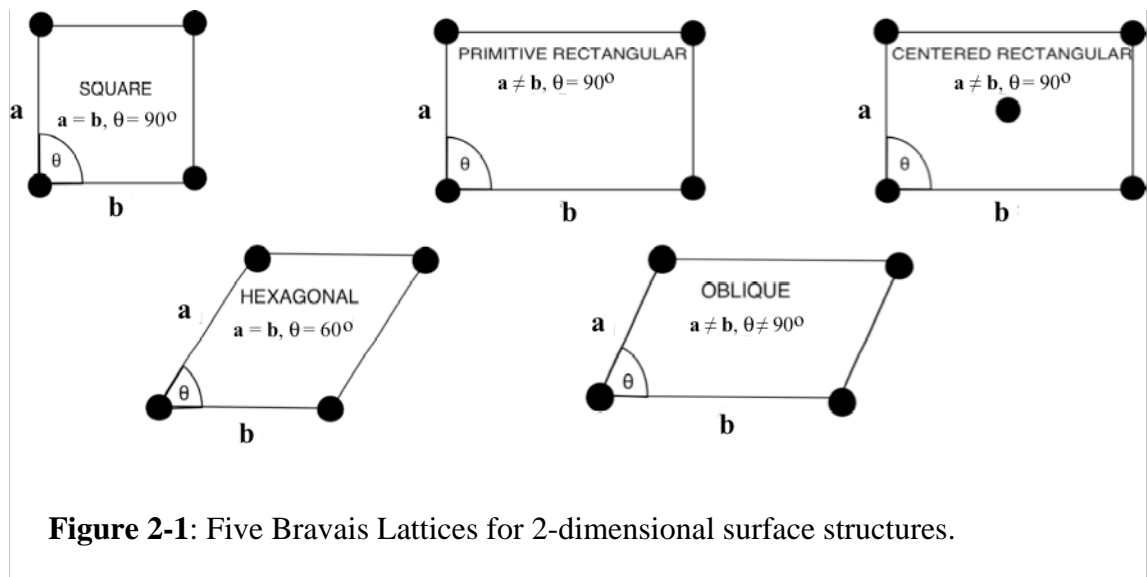


Figure 2-1: Five Bravais Lattices for 2-dimensional surface structures.

B. THE Cr(110) SURFACE

Chromium crystallizes in the body-centered cubic (BCC) structure.²⁷ The BCC structure consists of atoms located at the corners of a cube and one atom located at the center of the cube. The lattice constant for a cubic crystal is defined as the length of the sides of the cube and is $a_0 = 2.88 \text{ \AA}$ for chromium, as seen in Figure 2-2a. The (110) surface of chromium forms a centered rectangular lattice with dimensions $a_1 = a_0$ and $a_2 = \sqrt{2}a_0$, as shown in Figure 2-2b. This surface is quasi-hexagonal with lattice constants $a_1' = a_0$ and $a_2' = \frac{\sqrt{3}}{2}a_0 = 0.866 a_0$ with both lattice vectors separated by an angle $\beta = 125^\circ$, as shown in Fig. 2-2c. For a true hexagonal lattice both lattice constants would have the same distance and would be separated by an angle of 120° .

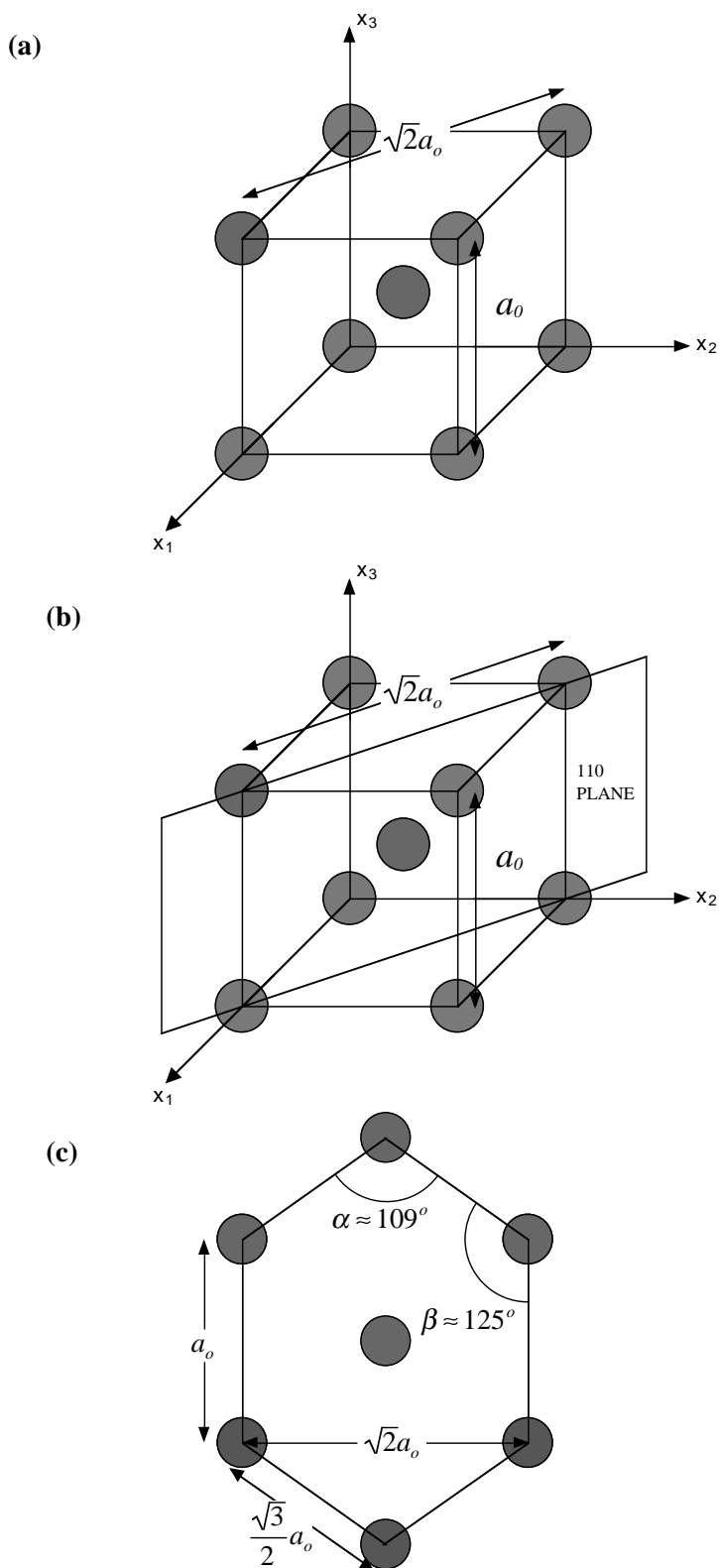


Figure 2-2: Schematic of chromium (Cr). The (a) body-centered cubic, BCC, crystal with lattice constant $a_0 = 2.88 \text{ \AA}$, the (b) (110) plane with lattice constants a_0 and $\sqrt{2}a_0$, and the (c) quasi-hexagonal surface with lattice constants a_0 and $(\sqrt{3}/2)a_0$.

C. THE $\text{Cr}_2\text{O}_3(0001)$ SURFACE

Chromium oxide (Cr_2O_3) crystallizes in the corundum structure.²⁷ This structure is a hexagonal lattice, which can be viewed as an ABAB stacking of close-packed layers of oxygen atoms with a hexagonal arrangement of chromium atoms on either side of the oxygen layers. The chromium atoms form a $(\sqrt{3} \times \sqrt{3}) R30^\circ$ arrangement with respect to the close-packed oxygen sublattice, as shown in Figure 2-3a. The chromium layers on either side of the oxygen plane are shifted laterally with respect to each other, as shown in Fig. 2-3b. The lattice constants of Cr_2O_3 are $a_0 = 4.95 \text{ \AA}$ and $c_0 = 13.58 \text{ \AA}$, which corresponds to six oxygen stacking planes.

The oxidation of the $\text{Cr}(110)$ surface results in the formation of an epitaxial $\text{Cr}_2\text{O}_3(0001)$ overlayer structure. The close-packed oxygen sublattice is reasonably well lattice matched to the $\text{Cr}(110)$ surface. The oxygen-oxygen nearest-neighbor distance is $a_{Ox} = a_0/\sqrt{3} = 2.86 \text{ \AA}$; whereas, the chromium-chromium next-nearest-neighbor distance is $a_1' = a_0 = 2.88 \text{ \AA}$. This results in a lattice mismatch of only -0.7% in the $[100]$ direction.

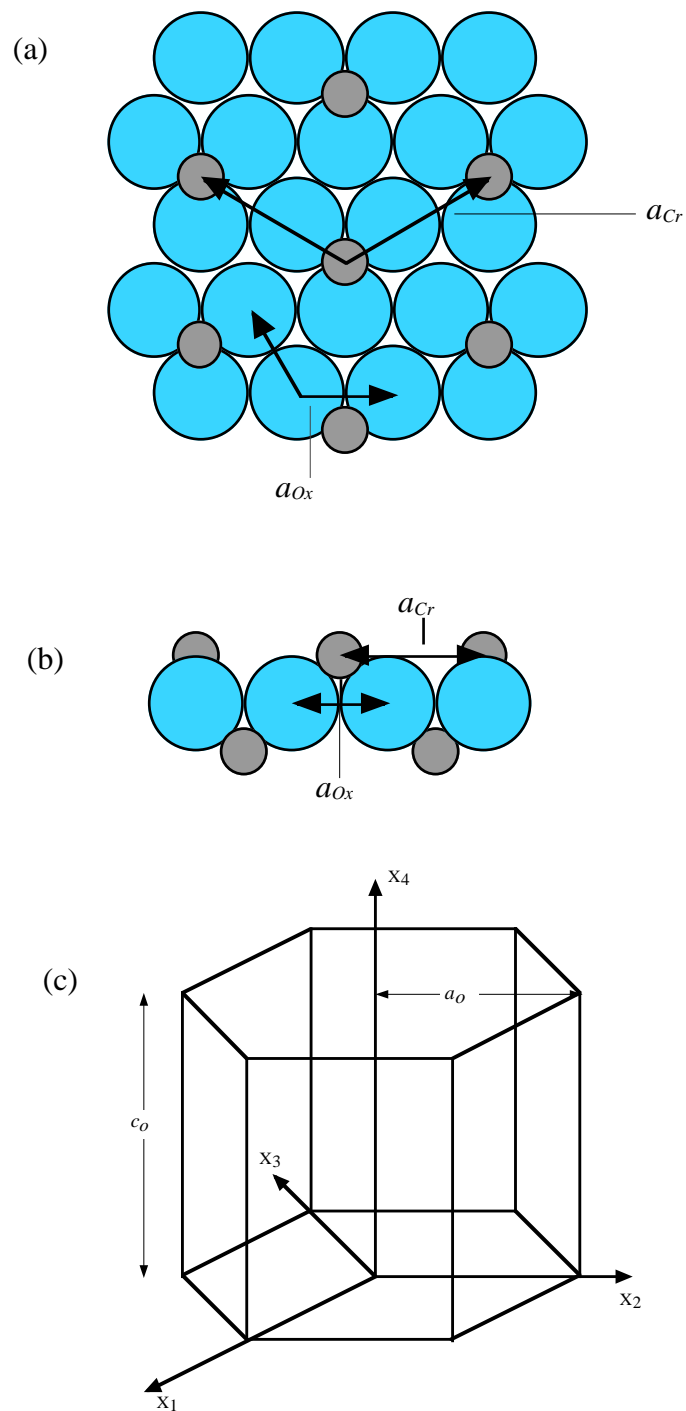


Figure 2-3: Schematic of $\text{Cr}_2\text{O}_3(0001)$ crystal. The (a) top view of $\text{Cr}_2\text{O}_3(0001)$ surface, the (b) side view of $\text{Cr}_2\text{O}_3(0001)$ surface, where the blue circles represent oxygen atoms and the grey circles represent chromium atoms, and the (c) the conventional cell of the hexagonal lattice.

D. ELECTRON DIFFRACTION FROM A CRYSTAL SURFACE

To derive information about the real crystal structure from the related LEED pattern, a relationship must be established between the reciprocal lattice structure and the real lattice structure. The diffraction pattern obtained from LEED analysis represents the reciprocal lattice structure. The diffraction pattern is generated from the constructive interference of scattered electrons. The scattered electrons originate from the interaction between the electron beam and the atoms of the crystal. The electron beam-atom interaction can be compared to the interaction between an incident plane wave and a collection of spherical scattering centers.²⁸ The plane wave that represents the incident electron beam can be defined as a wave function

$$\Psi(\mathbf{r}, t) = Ae^{i(\mathbf{k}_o \cdot \mathbf{r}' - \omega t)}, \quad [2-2]$$

where \mathbf{k}_o is the wave vector of the incident electron beam, \mathbf{r} is the position vector of the plane at incidence, and ω is the angular frequency. If the incident electron beam scatters from one electron, as shown in Figure 2-4, the scattered wave-function can be expressed as

$$\Psi(\mathbf{r}, t) = f_e \frac{A}{|\mathbf{r}' - \mathbf{r}|} \left[e^{i\mathbf{k}' \cdot (\mathbf{r}' - \mathbf{r}) - \omega t} \right], \quad [2-3]$$

where $|\mathbf{r}' - \mathbf{r}|$ is the electron-detector distance,^{29,30} A is the amplitude of the incident wave, \mathbf{r} is the radial distance from an arbitrary origin to the electron, and \mathbf{r}' is the radial distance from the same arbitrary origin to a detector, \mathbf{k}' is the scattered wave vector, and f_e is the

electron scattering length and is proportional to the incident wave by a factor of $e^{ik_o \cdot r'}$.

Disregarding the constant of proportionality, expression [2-2] can then be rewritten as

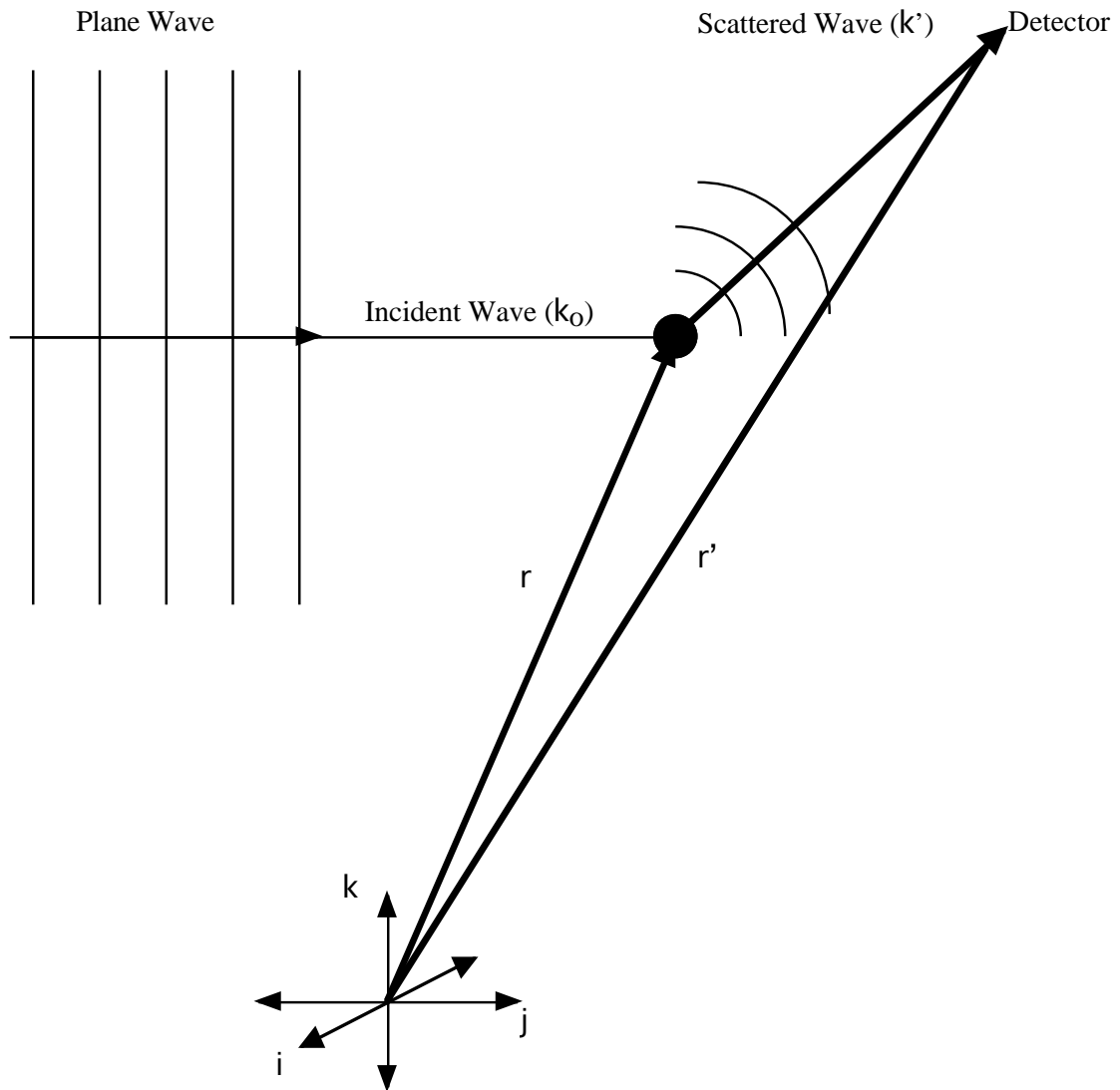


Figure 2-4: Plane wave incident on a spherical scattering center. Wave vector k_o , incident on a spherical scattering center at r and scattered wave, with wave vector k' , detected at r' from an arbitrary origin in space.

$$\Psi(\mathbf{r}, t) = \frac{A}{|\mathbf{r}' - \mathbf{r}|} e^{i\Delta\mathbf{k} \cdot \mathbf{r}} \left[e^{i\mathbf{k}' \cdot (\mathbf{r} - \mathbf{r}') - \omega t} \right], \quad [2-4]$$

where $\Delta\mathbf{k} = \mathbf{k}_0 - \mathbf{k}'$ ^{25, 26, 29, 30} is the difference in wave vector between the incident and scattered wave respectively and $(\mathbf{k}_0 - \mathbf{k}') \cdot \mathbf{r}'$ is the phase difference.^{29, 30} Applying the same formulism to the case of the plane wave incident on two electrons, expression [2-4] becomes

$$\Psi(\mathbf{r}, t) = \frac{A}{|\mathbf{r} - \mathbf{r}^*|} e^{i(\mathbf{k}' \cdot \mathbf{r}' - \omega t)} \left[e^{-i\Delta\mathbf{k} \cdot \mathbf{r}_1} + e^{-i\Delta\mathbf{k} \cdot \mathbf{r}_2} \right], \quad [2-5]$$

where $\mathbf{r} - \mathbf{r}^* = \mathbf{r} - \mathbf{r}_1 = \mathbf{r} - \mathbf{r}_2$ since the electrons are approximately equidistant from the detector,³⁰ \mathbf{r}_1 and \mathbf{r}_2 are position vectors from the origin to electrons in position P_1 and P_2 respectively.²⁹ For elastic collision where $|\mathbf{k}'| = |\mathbf{k}|$, the phase difference, δ , is then

$$\delta = (\mathbf{D} \cdot \mathbf{S}' - \mathbf{D} \cdot \mathbf{S}_o) k = (\overline{P_2N} - \overline{P_2M}) 2\pi / \lambda, \quad [2-6]$$

where \mathbf{D} is $\mathbf{r}_1 - \mathbf{r}_2$, and $(\overline{P_2N} - \overline{P_2M})$ is the path length difference between the wave incident at P_1 and the incident wave at P_2 as can be seen in Figure 2-5 below.

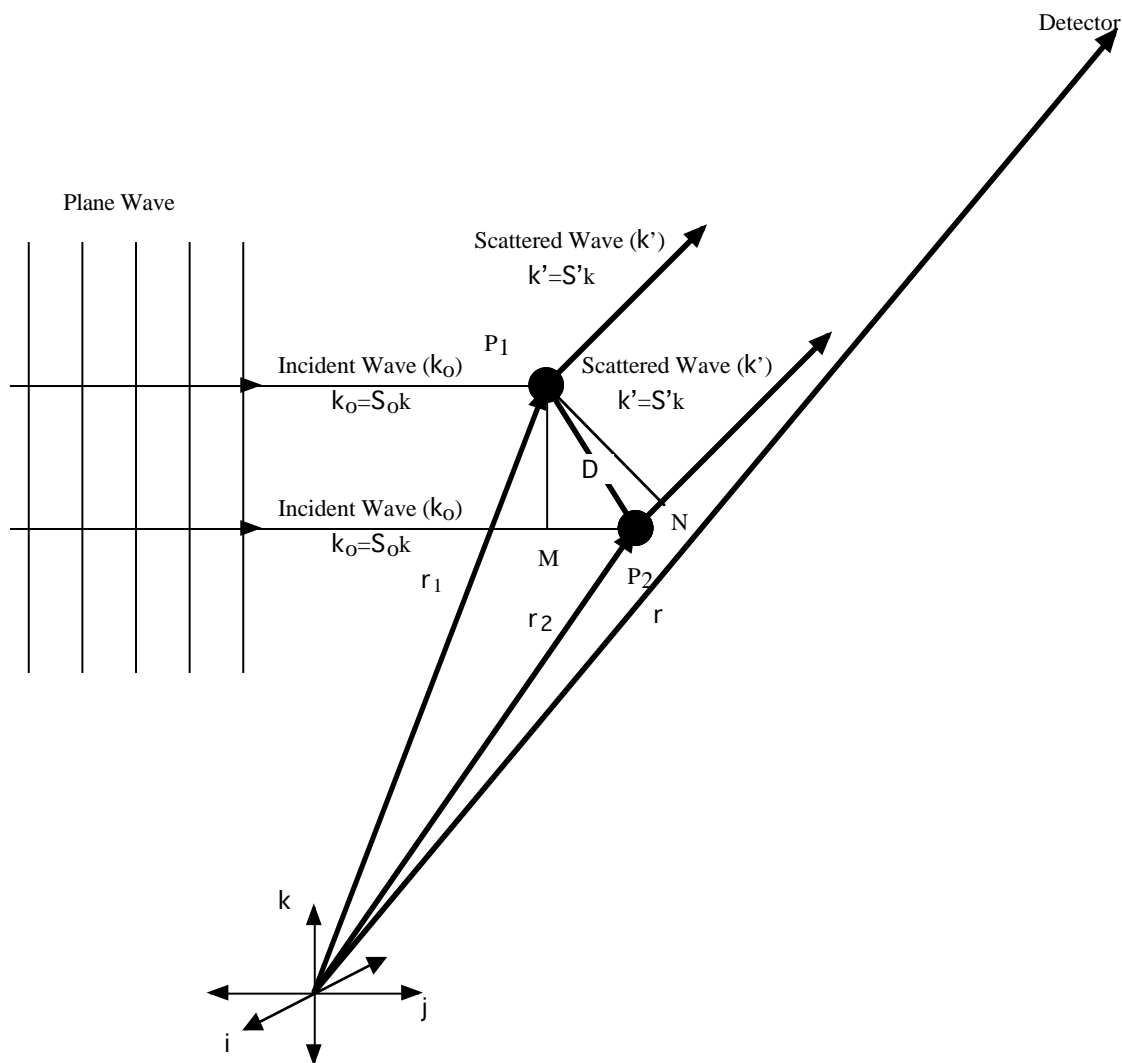


Figure 2-5: Electron plane wave scattering from two electrons. Electron beam scattering from two electrons at P_1 and P_2 , where \mathbf{k}_0 and \mathbf{k}' are wave vectors of the incident and scattered waves, respectively, and D is the separation of the electrons at P_2 and P_1 .

Physically, the observable quantity is the intensity, or

$$\Psi^*(\mathbf{r}, t)\Psi(\mathbf{r}, t) = \frac{|A|^2}{|\mathbf{r}' - \mathbf{r}|^2} \left[e^{i\Delta\mathbf{k} \cdot (\mathbf{r}_1 - \mathbf{r}_2)} + e^{-i\Delta\mathbf{k} \cdot (\mathbf{r}_1 - \mathbf{r}_2)} + 2 \right] \quad [2-7]$$

which can be restated as

$$\Psi^*(\mathbf{r}, t)\Psi(\mathbf{r}, t) = 4|A|^2 \cos^2 \left[\frac{1}{2} \Delta\mathbf{k} \cdot (\mathbf{r}_1 - \mathbf{r}_2) \right]. \quad [2-8]$$

It is then evident from [2-8] that only for integer multiples of 2π for the argument of the \cos^2 function is the intensity a maximum. For the more general case of scattering from an atom, the scattered wave function is evaluated as a volume integral over the electron density, $\rho(r')$, surrounding the atom at a distance \mathbf{r}' from the atom,^{29, 30}

$$\Psi(\mathbf{r}, t) = \frac{A}{|\mathbf{r}' - \mathbf{r}|} e^{i(k' \cdot \mathbf{r} - \omega t)} \int_{\tau} e^{-i\Delta\mathbf{k} \cdot \mathbf{r}'} \rho(r') d\tau. \quad [2-9]$$

Using expression [2-7] over all the atoms in a crystal yields a scattered wave function defined as

$$\Psi(\mathbf{r}, t) = \frac{A}{|\mathbf{r}' - \mathbf{r}|} e^{i(k' \cdot \mathbf{r} - \omega t)} \sum_j e^{-i\Delta\mathbf{k} \cdot \mathbf{r}_j} \int_{\tau} e^{-i\Delta\mathbf{k} \cdot \mathbf{r}''} \rho(r'') d\tau, \quad [2-10]$$

where the summation accounts for all the atoms in the $\mathbf{r}_{j^{\text{th}}}$ position with respect to an origin and the integral is for all the electrons at a distance \mathbf{r}'' from the atom, Figure 2-6.

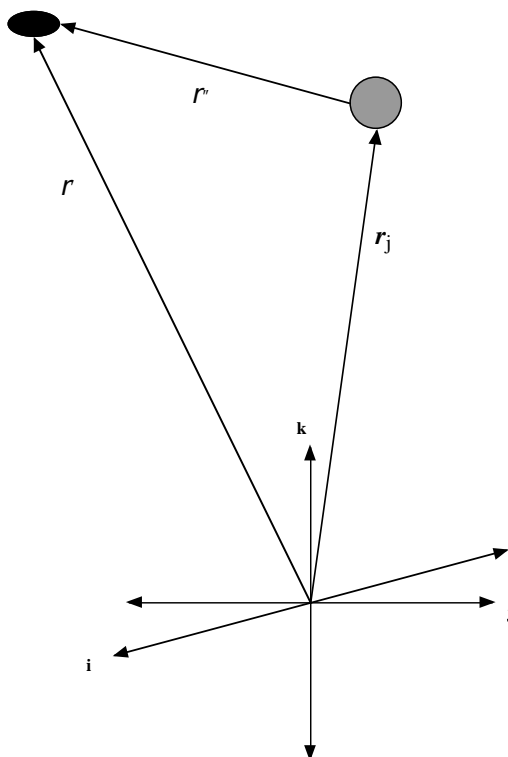


Figure 2-6: Coordinate system and position vectors of electron cloud and j^{th} atom. The grey circle represents the j^{th} atom at position \mathbf{r}_j and the black oval represents an electron cloud at a position \mathbf{r}' . The distance from the j^{th} atom to the electron is $\mathbf{r}'' = \mathbf{r}' - \mathbf{r}_j$.

The integral part of the wave function of equation [2-10] is known as the atomic scattering factor, f_a .²⁹ The position of an atom in a crystal is defined by its basis vectors and is invariant under a transformation \mathbf{T}_m , that is $\mathbf{r}_j = n_1 \mathbf{a} + n_2 \mathbf{b} + n_3 \mathbf{c} + \mathbf{T}_m$ ⁷ such that the scattered wave-function takes the form

$$\Psi(\mathbf{r}, t) = \frac{A}{|\mathbf{r} - \mathbf{r}'|} (f_a) e^{i(\mathbf{k}' \cdot \mathbf{r} - \omega t)} \sum_{n_1} \sum_{n_2} \sum_{n_3} \sum_m e^{-i\Delta\mathbf{k} \cdot (n_1 \mathbf{a} + n_2 \mathbf{b} + n_3 \mathbf{c} + \mathbf{T}_m)}, \quad [2-11]$$

where the sum over \mathbf{T}_m is over the unit cell and is known as the geometrical structure factor, F ,²⁹ and the sum over $n_1 \mathbf{a} + n_2 \mathbf{b} + n_3 \mathbf{c}$ is over the unit cells of the crystal and is known as the lattice structure factor, S .²⁹ Regarding only the lattice structure factor, it has a geometric sum of the form

$$S = \left\{ \frac{\sin(1/2 N \Delta\mathbf{k} \cdot \mathbf{a})}{\sin(1/2 \Delta\mathbf{k} \cdot \mathbf{a})} \right\} \times \left\{ \frac{\sin(1/2 N \Delta\mathbf{k} \cdot \mathbf{b})}{\sin(1/2 \Delta\mathbf{k} \cdot \mathbf{b})} \right\} \times \left\{ \frac{\sin(1/2 N \Delta\mathbf{k} \cdot \mathbf{c})}{\sin(1/2 \Delta\mathbf{k} \cdot \mathbf{c})} \right\}, \quad [2-12]$$

where the crystal has N unit cells along the \mathbf{a} , \mathbf{b} , and \mathbf{c} axes.²⁹ Again, the intensity is the observed quantity; therefore, the modulus squared of the wave function is approximately

$$\Psi^*(\mathbf{r}, t) \Psi(\mathbf{r}, t) = |A|^2 \left\{ \frac{\sin^2(1/2 N \Delta\mathbf{k} \cdot \mathbf{a})}{\sin^2(1/2 \Delta\mathbf{k} \cdot \mathbf{a})} \right\} \times \left\{ \frac{\sin^2(1/2 N \Delta\mathbf{k} \cdot \mathbf{b})}{\sin^2(1/2 \Delta\mathbf{k} \cdot \mathbf{b})} \right\} \times \left\{ \frac{\sin^2(1/2 N \Delta\mathbf{k} \cdot \mathbf{c})}{\sin^2(1/2 \Delta\mathbf{k} \cdot \mathbf{c})} \right\} \quad [2-13]$$

where, for the limiting case, a maximum intensity of order N^2 is found only for values of

$$\Delta \mathbf{k} \cdot \mathbf{a} = 2\pi h_1, \quad [2-14]$$

$$\Delta \mathbf{k} \cdot \mathbf{b} = 2\pi h_2, \quad [2-15]$$

$$\Delta \mathbf{k} \cdot \mathbf{c} = 2\pi h_3, \quad [2-16]$$

which are known as the Laue equations^{25, 26, 29} for integer values of h_1 , h_2 and h_3 .

Three vectors that satisfy the Laue equations are^{25, 29, 30}

$$\mathbf{B}_1 = 2\pi \frac{\mathbf{b} \times \mathbf{c}}{\mathbf{a} \cdot (\mathbf{b} \times \mathbf{c})}, \quad [2-17]$$

$$\mathbf{B}_2 = 2\pi \frac{\mathbf{c} \times \mathbf{a}}{\mathbf{a} \cdot (\mathbf{b} \times \mathbf{c})}, \quad [2-18]$$

$$\mathbf{B}_3 = 2\pi \frac{\mathbf{a} \times \mathbf{b}}{\mathbf{a} \cdot (\mathbf{b} \times \mathbf{c})}, \quad [2-19]$$

and $\Delta \mathbf{k}$ can be defined as

$$\Delta \mathbf{k} = h_1 \mathbf{B}_1 + h_2 \mathbf{B}_2 + h_3 \mathbf{B}_3, \quad [2-20]$$

which is known as the Laue condition.³⁰ Vectors that satisfy the Laue condition are called reciprocal lattice vectors, and when applied to the Laue equations yield terms of the kind

$$\mathbf{a} \cdot \mathbf{B}_1 = 2\pi \quad [2-21]$$

$$\mathbf{b} \cdot \mathbf{B}_2 = 2\pi \quad [2-22]$$

$$\mathbf{c} \cdot \mathbf{B}_3 = 2\pi \quad [2-23]$$

E. CONSTRUCTING THE RECIPROCAL LATTICE OF Cr(110)

As mentioned previously, Cr crystallizes as a BCC. The Cr(110) plane is quasi-hexagonal with real lattice constants defined as,

$$\mathbf{a} = a\hat{i}, \quad [2-24]$$

$$\mathbf{b} = -a/\sqrt{2}\hat{i} + a/\sqrt{2}\hat{j}, \quad [2-25]$$

$$\mathbf{c} = \hat{k}, \quad [2-26]$$

where \mathbf{c} is a unit vector in \hat{k} since this is a surface experiment, Figure 2-7. The calculated reciprocal lattice constants using 2-17 – 2-19 in conjunction with 2-21 – 2-23 are,

$$\mathbf{B}_1 = 2\pi\left(\frac{\sqrt{2}}{2a}\hat{j} + \frac{1}{\sqrt{2}a}\hat{i}\right), \mathbf{B}_2 = 2\pi\left(\frac{\sqrt{2}}{a}\hat{j}\right), \mathbf{A}_3 = 2\pi\hat{k}, \text{ figure 2-8.} \quad [2-27]$$

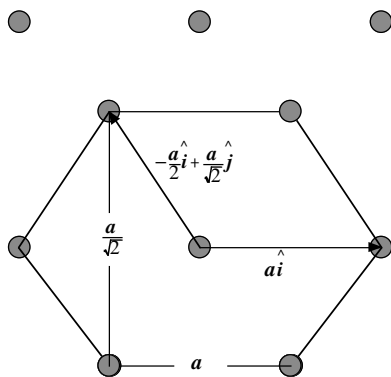


Figure 2-7: Theoretical real lattice drawing of Cr(110).

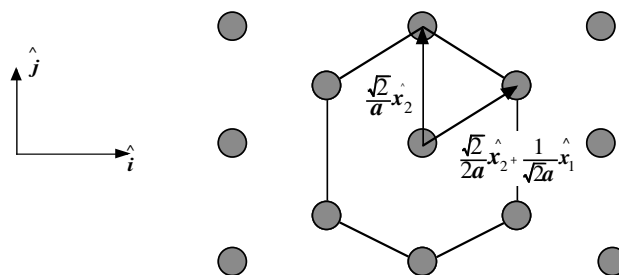


Figure 2-8: Theoretical reciprocal lattice drawing of Cr(110) based on the Laue condition.

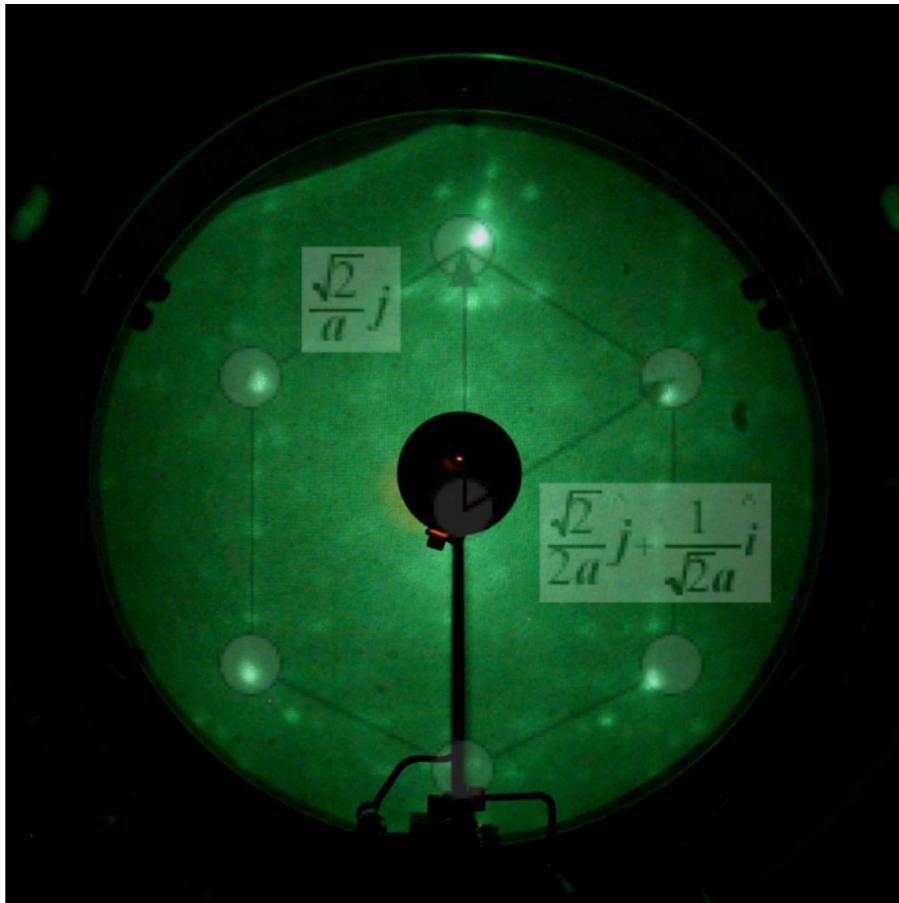


Figure 2-9: Observed LEED image of Cr(110) at room temperature with overlaid theoretical reciprocal lattice of Cr(110). The image demonstrates the correlation between the theoretical image derived from the Laue equations and the pattern observed with LEED.

CHAPTER III

EXPERIMENTAL TECHNIQUES

A. ULTRA HIGH VACUUM

Ultra high vacuum (UHV) conditions are satisfied when a pressure of 1×10^{-9} Torr or lower is achieved. Under UHV conditions, a clean surface can be analyzed without the influence of contamination from the residual gasses in the chamber for several hours.²⁶ A typical 3-dimensional solid will have a density of $\sim 10^{23}$ atoms/cm³; whereas, a typical 2-dimensional surface will have $\sim 10^{15}$ atoms/cm².²⁶ For instance, the bulk atomic density of Cr is $n_{bulk} = 8.4 \times 10^{22}$ cm⁻³ and the atomic density of the (110) surface is $\sigma_{(110)} = 1.7 \times 10^{15}$ cm⁻². The atoms at a surface have a lower coordination than those in the bulk. In other words, the surface atoms interact with other atoms in the plane of the surface and below the surface. The fact that there are no atoms above the surface with which to interact can result in changes of the chemical, electronic, and magnetic properties of the surface atoms when compared to the atoms within the bulk of the crystal.

For a dilute gas, the molecules have a Maxwell-Boltzmann average thermal velocity, \bar{v} , defined as

$$\bar{v} = \sqrt{\frac{8kT}{\pi m}}, \quad [3-1]$$

where $k = 1.38 \times 10^{-23} \frac{J}{K}$ is the Boltzmann constant, T is the absolute temperature in Kelvin, and m is the molecular mass (*e.g.*, 32 amu for O₂). The atoms impinge on a square centimeter of the surface at an average flux, Φ_g , defined as

$$\Phi_g = \frac{1}{4} n \bar{v} \quad [3-2]$$

where $n = \frac{N}{V}$ is the number of gas molecules per unit volume. Substituting the expression for the average thermal velocity into the expression for the flux and assuming that the gas acts as an ideal gas,

$$PV = NkT, \quad [3-3]$$

where P is the pressure in Torr, V is the volume in cm³, and N is the number of gas molecules, the incident flux can be defined as ²⁶

$$\Phi_g = \frac{P}{\sqrt{2\pi mkT}} = 3.5 \times 10^{22} \frac{P}{\sqrt{mT}} \text{ (molecules} \cdot \text{cm}^{-2} \cdot \text{s}^{-1}\text{)}. \quad [3-4]$$

Therefore, the incident particle flux is directly proportional to the pressure for a given temperature T . To reduce surface contamination from surrounding gas molecules, a low pressure must be maintained.

When molecules impinge on a surface, some of them will bind to the surface, which is called adsorption, and some will interact weakly and return to the gas phase. Therefore, one can define a sticking coefficient, S , which is the probability that an impinging molecule binds to the surface. As previously stated, a crystalline surface has approximately 10^{15} adsorption sites per square centimeter. If a diatomic gas molecule adsorbs on the surface dissociatively, a flux of 5×10^{14} molecules \cdot cm $^{-2}$ \cdot s $^{-1}$ will result in the formation of a monolayer on the surface within approximately one second if the sticking coefficient S is unity. For oxygen ($m = 32$ amu) at room temperature ($T = 300$ K), the pressure dependent flux is

$$\Phi_{O_2} = 3.6 \times 10^{20} P \text{ (molecules} \cdot \text{cm}^{-2} \cdot \text{s}^{-1}\text{)}. \quad [3-5]$$

For reactive surfaces where the sticking coefficient is close to one, an oxygen pressure of 10^{-6} Torr will result in the formation of a monolayer of atomic oxygen on a surface within approximately one second.

For surface science studies, the amount of gas molecules dosed onto a surface is measured in units of Langmuir, which is defined as

$$1 L = 1 \times 10^{-6} \text{ Torr}\cdot\text{s}. \quad [3-6]$$

Therefore, a dose of one L will produce approximately a monolayer of adsorbed gas molecules on a reactive surface at room temperature. The time to form a monolayer of gas molecules on a surface is given by

$$\tau \approx \frac{10^{-6}}{S \cdot P} \text{ (seconds)}. \quad [3-7]$$

From Eqtn. 3-7, it can be seen that at a pressure of 10^{-6} Torr a new monolayer will form every second on reactive surfaces. However, at a pressure of 10^{-10} Torr it will take at least 10,000 s (~3 hr) to form a monolayer of adsorbed gas molecules on the surface. It then becomes evident that surface analysis should be performed under UHV conditions to prevent the influence of surface contamination from gases within the vacuum chamber.

B. VACUUM TECHNIQUES

The measurements for this thesis project were performed in a stainless steel UHV chamber. This UHV chamber with pumps, quadrupole mass spectrometer, and x,y,z , manipulator is shown in Figure 3-1 and Figure 3-2. The pressure was maintained by a combination of vacuum pumps. A rotary vane pump, which is an oil lubricated compression pump, can achieve pressures as low as 1×10^{-3} Torr. The pump has a zeolite trap to capture oil that would diffuse into the UHV chamber, causing contamination of the system. The rotary vane pump is connected to a turbo molecular pump, which is then connected directly to the UHV chamber. In other words, the rotary vane pump backs the turbo molecular pump. The turbo molecular pump has a series of fan blades that rotate at frequencies of roughly 60,000 rpm and pump gases in the chamber by momentum transfer. The turbo molecular pump can achieve a pressure as low at 10^{-11} Torr if a backing pressure of 10^{-3} Torr is maintained. The UHV chamber also has an ion pump and a titanium sublimation pump (TSP). The ion pump works by field emitting electrons from titanium plates into central electrodes, which can cause ionization of gas molecules within the pump. Once the gas molecules are ionized, they are accelerated towards the titanium plates, where they imbed in the titanium and are reactively pumped away. Large magnets are used to increase the pumping speed by causing the field emitted electrons to follow a helical path, which increases the probability of interacting with gas molecules in the pump. Since the molecules are captured by reacting with the titanium plates, ion pumps cannot be used for pumping inert gases such as argon or neon. The TSP uses a layer of clean titanium to pump reactive gases such as water and hydrogen. Titanium is evaporated from a titanium alloy

wire by resistance heating, which is known as flashing the TSP. The evaporated titanium sticks to the walls of the vacuum can that houses the TSP.

When the UHV system is initially pumped down from atmospheric pressure, the combination of the ion pump and the turbo molecular pump will only reduce the pressure to about 10^{-7} Torr initially. This is because there is a large flux of gas molecules, primarily water, desorbing from the walls of the vacuum chamber. To achieve UHV, the chamber and the pumps must be baked for at least 24 hours at an approximate temperature of 150 °C. After bake out, the base pressure for this UHV chamber was 4×10^{-11} Torr. Once UHV is achieved, the TSP is flashed for nearly 90 seconds at the start of every day before any work was carried out so that a fresh layer of titanium would be available to pump reactive gases in the chamber during the day. As a final note, besides creating a clean environment for studying crystal surfaces, UHV conditions also decrease the mean free path collision rate between residual gas molecules. This decrease provides an ideal environment where low energy electron diffraction (LEED) and temperature programmed desorption (TPD) analyses can be performed without interference with the residual gas molecules in the chamber.

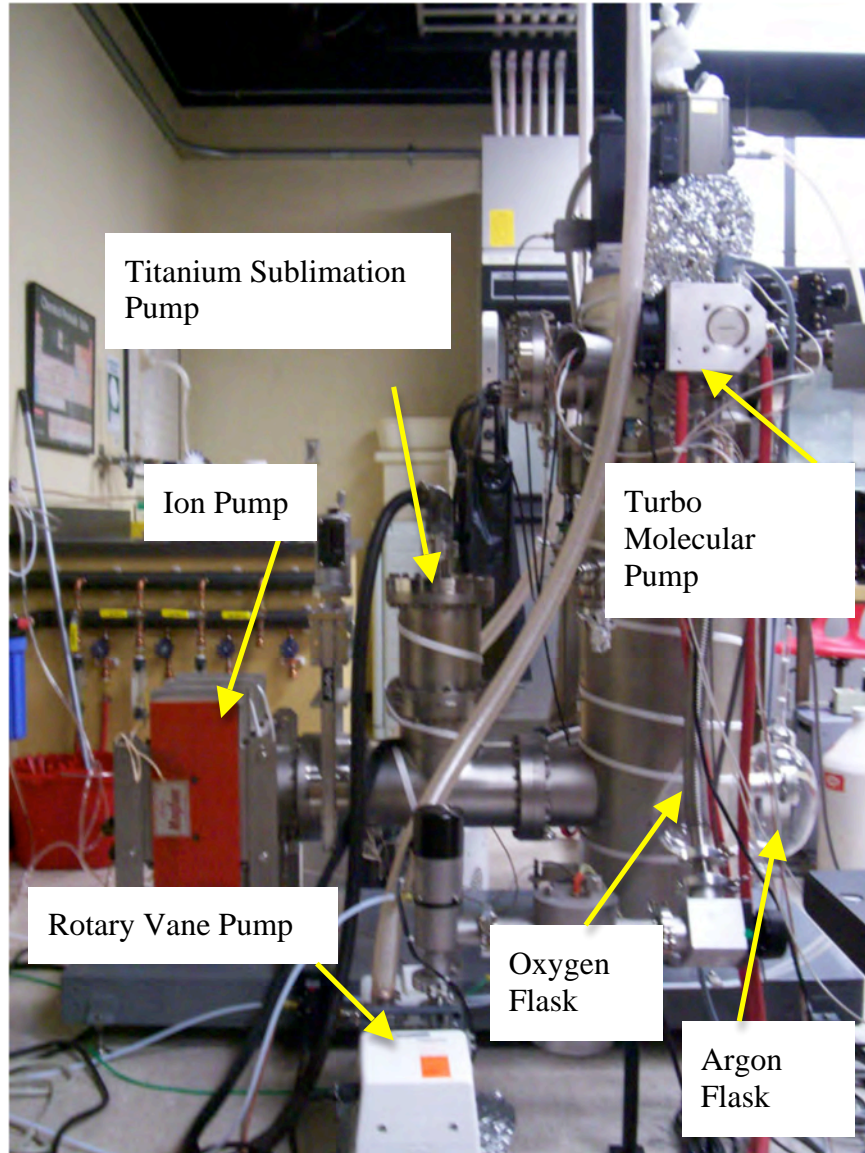


Figure 3-1: Ultra-High Vacuum chamber with pumping system labeled.

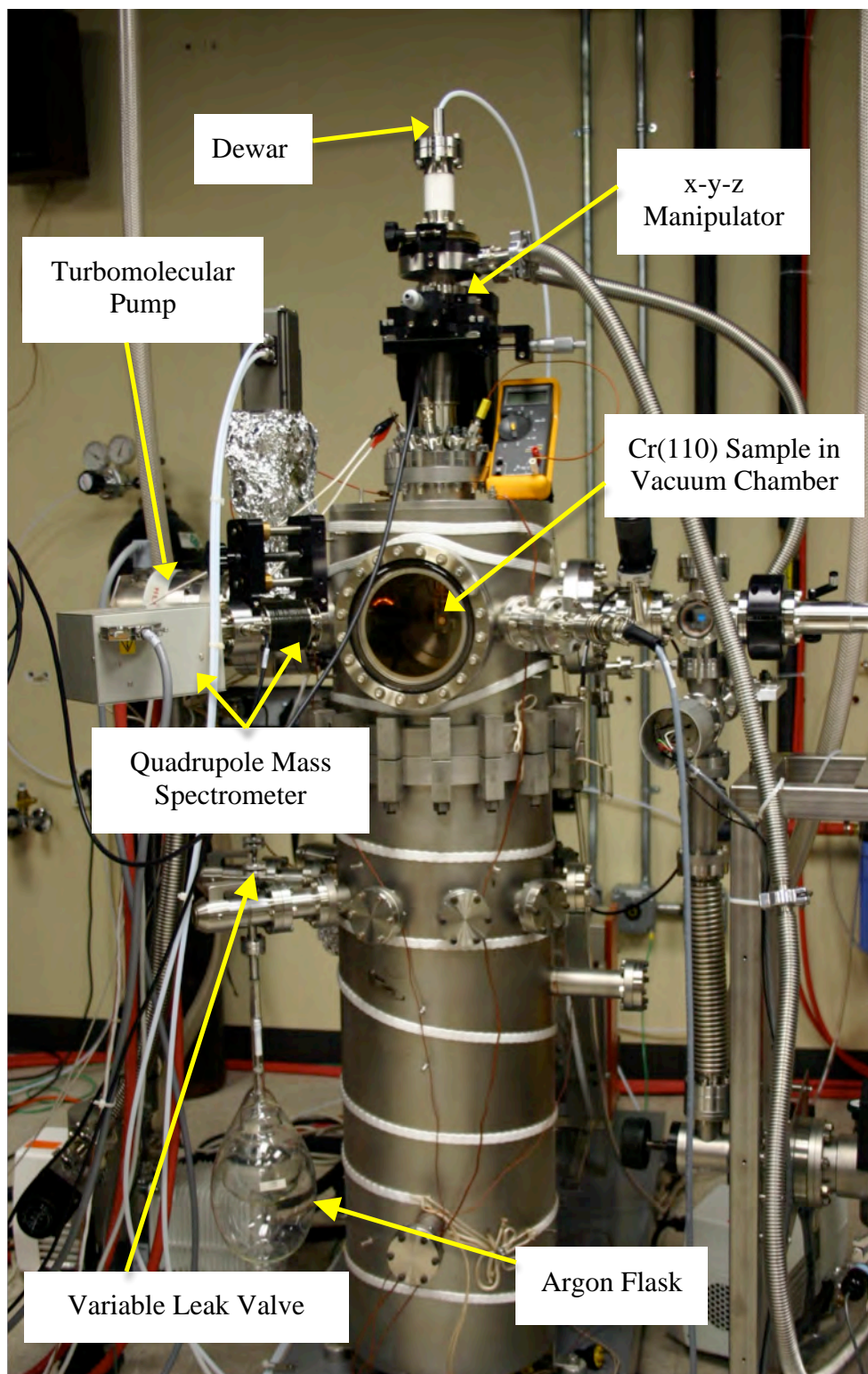


Figure 3-2: Ultra-High Vacuum chamber with quadrupole mass spectrometer and x,y,z manipulator. The oxygen flask is not seen since it is directly behind the argon flask.

C. LOW ENERGY ELECTRON DIFFRACTION OPTICS

The technique used to determine the surface crystal structure was low energy electron diffraction (LEED). A LEED optics consists of an electron gun to emit, accelerate and direct electrons towards a target crystal where the electrons then back-scatter, a series of hemispherical grids to reject the inelastically back-scattered electrons and to accelerate the elastically back-scattered electrons towards the detector, and a hemispherical fluorescent screen to detect the electrons. A schematic of the electron gun and the detector are shown in Figure 3-3.¹²

The electron gun for this experiment houses a Wehnelt cylinder that contains a heated filament for the thermionic emission electrons. The filament is biased negatively with respect to the grounded nozzle of the electron gun, so that the electrons leave the gun at ground potential with a kinetic energy of $E = eV_{fil}$. The nozzle of the electron gun and the crystal are both held at ground to prevent electron deflection by stray electric fields. In addition, the LEED optics are surrounded by a metal can made of μ -metal, which shields stray magnetic fields that can also deflect the electrons. The electrons are then incident on the crystal and back-scatter. The back-scattered electrons then come in contact with four grids. The first grid is held at ground to create an electric field-free region between the crystal sample and the fluorescent screen. The second and third grids are held at small negative potentials, with respect to the electron beam potential, and act to filter out the inelastically scattered electrons. The fourth grid is held at ground and the fluorescent screen is held at approximately 3kV. The elastic electrons are then accelerated between the fourth grid and the screen, acquiring an energy that allows light to be emitted when they strike the phosphorescent screen.

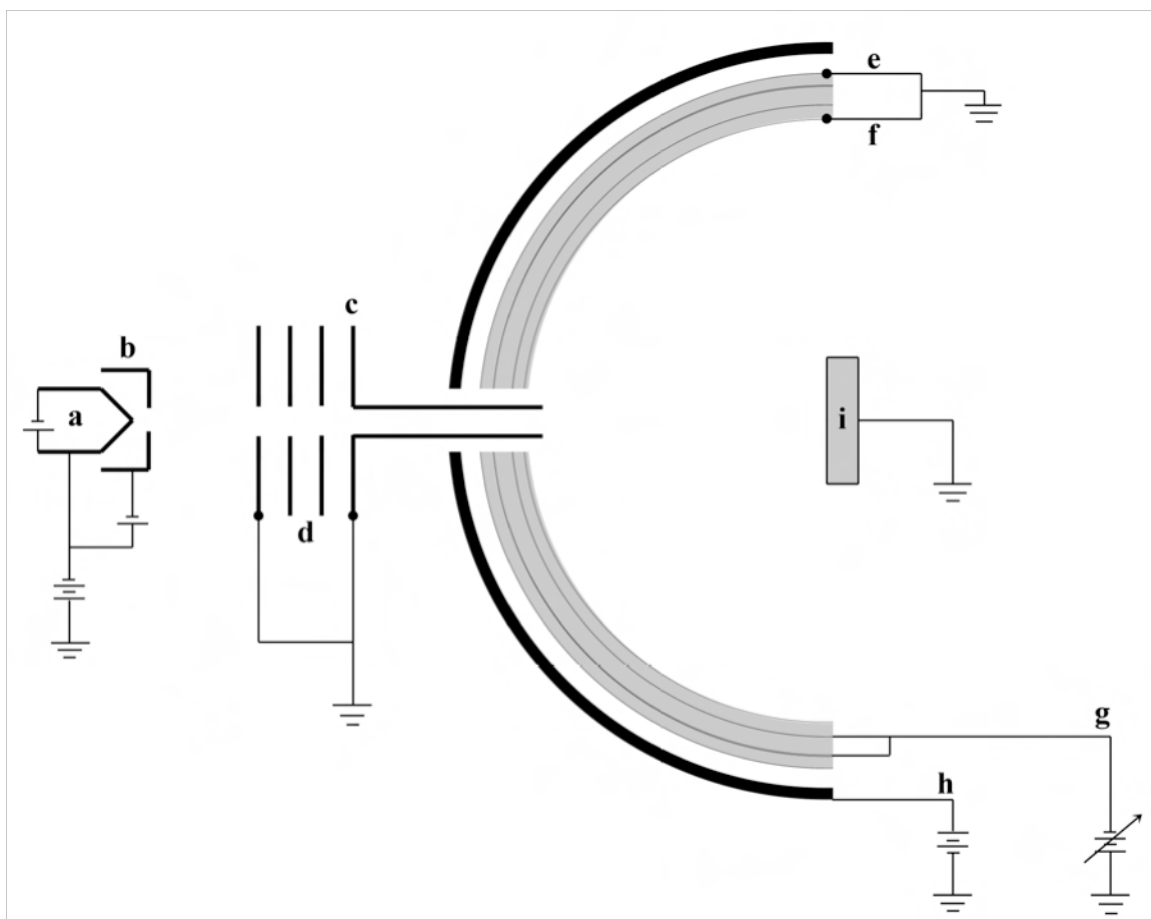


Figure 3-3: Schematic of electron gun and detector of LEED. The electron gun consists of (a) heater filament/cathode, (b) Wehnelt cylinder, (c) anode held at ground potential, and (d) focusing rings. The detector is composed of four hemispherical grids (e) and (f) held at ground potential, (g) held at a potential less than the accelerating potential to filter out inelastically scattered electrons, and (h) collector (phosphor screen) held at a potential between 2kV and 5kV. The sample (i) is held a ground potential.

D. CRYSTAL SAMPLE HOLDER

The crystal sample holder shown below in Figure 3-4 is made of oxygen free high conductivity (OFHC) copper. It is attached to a Dewar that is then attached to an x - y - z manipulator. The manipulator allows the tilt angle ϕ to be adjusted for crystal alignment. It also has a differentially pumped rotary motion feedthrough to allow rotation of the sample through a full $\theta = 360^\circ$, Figure 3-5 below. The Dewar can be manually filled with liquid nitrogen to cool the crystal to temperatures approaching 120 K. Compressed air can also be blown into the Dewar to prevent overheating of the sample holder during annealing of the crystal. The crystal is affixed to a molybdenum insert by two 0.005 inch tantalum wires that are spot welded to the edges of the crystal. The insert is fastened onto the copper sample holder by two molybdenum leaf springs. A type K (chromel-alumel) thermocouple is spot welded to the edge of the crystal so that its temperature can be monitored. The crystal can be radiatively heated from a tungsten filament located behind the molybdenum insert. The maximum temperature that can be achieved using this method is ~ 973 K. The crystal can also be heated using an electron beam by biasing the sample at +750V while running a current through the tungsten filament. This is generally a cleaner method of heating the sample since most of the power is dissipated by the electron beam as it interacts with the crystal. With radiative heating, most of the radiation is reflected off of the crystal and is eventually absorbed by the sample holder and the rest of the chamber. The main drawback of e-beam heating is that the heating rate is nonlinear, which can result in overheating of the sample if the filament current is too high.

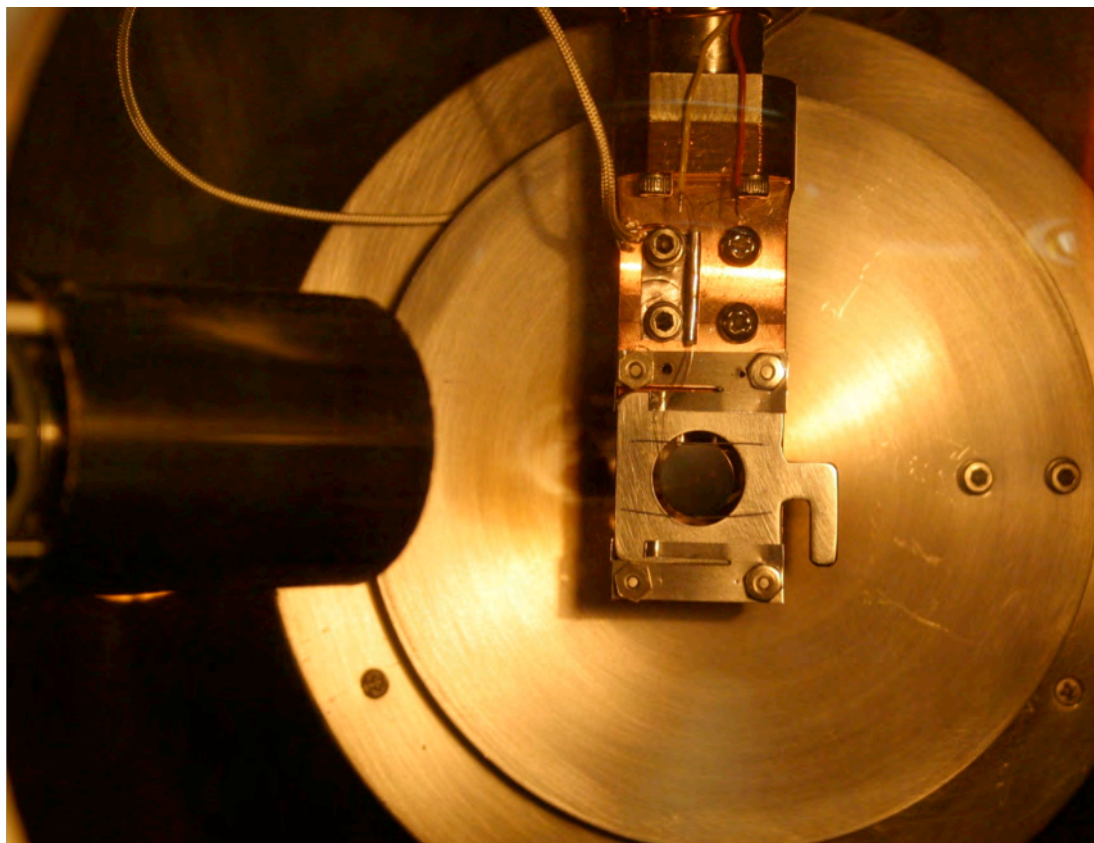


Figure 3-4: Interior view of ultra-high vacuum chamber. The image shows the (a) LEED shutter, the (b) quadrupole mass spectrometer detector, the (c) thermocouple leads, the (d) Cr(110) sample, the (e) Dewar, and the (f) sample holder.

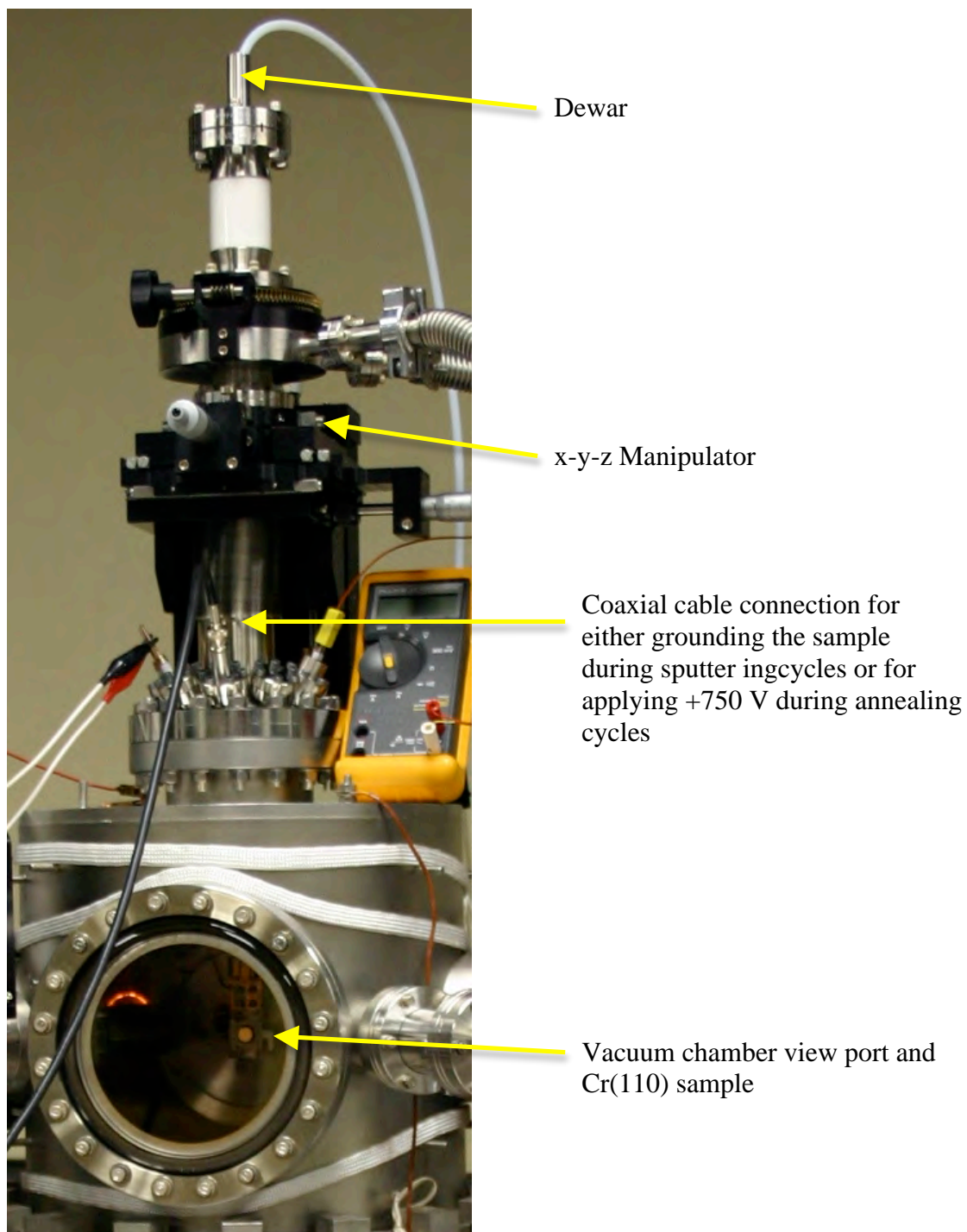


Figure 3-5: x,y,z manipulator and ultra-high vacuum chamber view port housing Cr(110) sample.

E. TEMPERATURE PROGRAMMED DESORPTION

Temperature programmed desorption (TPD) analysis is a technique used for measuring the interaction of gas molecules with a surface. With this technique, the activation energy for desorption, the desorption kinetics, and the relative coverage of the desorbing species can be determined. The TPD measurements consist of heating a sample, usually in a linear rate, while measuring the partial pressures of the desorbed molecules with a mass spectrometer. TPD analysis has become a standard investigative method in surface science experiments. Though it only divulges basic chemical processes of a surface, it can lead to results that require further investigation using more sophisticated instrumentation and theory. Though TPD studies were conducted as early as 1933 by Taylor and Langmuir, it was G. Ehrlich who first used TPD at low pressures and rapid heating rates to characterize the desorption kinetics of cesium on a tungsten substrate.³¹ P.A. Redhead adapted Ehrlich's method by using slower heating rates.³² The slower heating rates allowed Redhead to observe the existence of more binding states on surfaces and it also gave a linear dependence of temperature to time instead of the hyperbolic dependence that existed using Ehrlich's rapid heating rates.³¹ It is Redhead's slow heating rate method of TPD analysis that is used in this study.

The TPD system used to study the kinetics of the CO/Cr₂O₃(0001)/Cr(110) crystal is composed of a quadrupole mass spectrometer (QMS), which is also called a residual gas analyzer (RGA), a preamplifier, a data acquisition (DAQ) board, a computer, and a power supply for the heater filament. The preamplifier is used to amplify the thermocouple voltage, thus reducing noise. The DAQ board allows the computer to read the thermocouple voltage and to send a signal to control the filament power supply. Two

programs, which were written in LABView, were used for the TPD measurements. One program used a proportional feedback control to create the constant heating rate and collect the temperature vs. time data. The other program collected the partial pressure vs. time data.³³

The QMS measures the mass to charge ratio m/z of ionized atoms and molecules. The desorbed CO molecules from the $\text{Cr}_2\text{O}_3(001)/\text{Cr}(110)$ surface are ionized by a beam of 70 eV electrons at the front section of the QMS. The ionized gas is then accelerated through a potential field towards four electrically charged rods. A DC source and a radio frequency (RF) source are connected to the rods.²⁶ Each pair has its own DC and RF source associated with it, with the DC signal superimposed on the RF signal. The pairs of rods are at equal and opposite potentials. The RF source is swept over a frequency spectrum and serves as a discriminator, since at given radio frequencies only ions with a certain characteristic mass to charge ratio m/z will resonate through the rods and be detected as seen below in the figure 3-6.³⁵

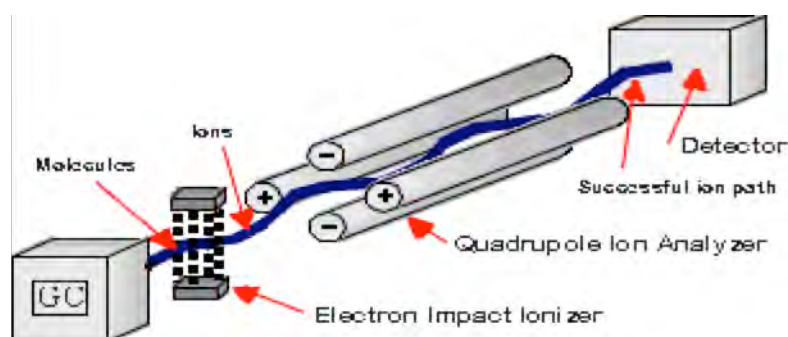


Figure 3-6: Schematic of quadrupole mass spectrometer (QMS)

The thermocouple signal is amplified by a preamp with a gain of $G = 101$ to increase the signal to noise level. A LABView program was used to read in the temperature of the crystal and to send a signal to the filament power supply to ramp up the temperature of the crystal, thus creating a temperature vs. time file. The conversion of the thermocouple voltage to a temperature was achieved by using two different polynomial conversion factors: one for 73 K to 273 K and another from 273 K to 773 K.³⁵ A linear heating rate was achieved using a proportional feedback control. In addition to the heating rate, the temperature ramp program also controls the maximum input current to the sample filament, maximum execution time, time delay between data collection points, and maximum sample temperature. A second LABView program was used to measure the partial pressures of up to eight different types of molecules, creating a partial pressure vs. time file. The communication between the QMS controller and the computer was done via the COM port of the computer. The programs graphically display the acquired data in real time, making it possible to visually ensure that the temperature increase is linear with time and to see the partial pressures of the desorbing gas molecules. Though the programs had already been created for a previous study,³³ the temperature control program had to be modified to detect temperatures below 273 K by adding a second polynomial conversion factor.

F. ANALYSIS OF ACTIVATION ENERGY USING TPD ANALYSIS

One of the main goals of this experiment is to measure the activation energy for the desorption of CO from the $\text{Cr}_2\text{O}_3(0001)/\text{Cr}(110)$ surface. As previously stated, the TPD analysis for this study uses the slow heating rate method that P.A. Redhead developed.³² The rate of desorption of molecules from a surface is given by the Polanyi-Wigner expression

$$r(\theta) = -\frac{d\theta}{dt} = -v_n \times e^{-\frac{E_a}{RT}} \times \theta^n, \quad [3-8]$$

where θ is the fractional surface coverage, E_a is the activation energy, v_n is a pre-exponential factor indicating the number of attempts of desorption a molecule undergoes per second, R is the ideal gas constant, T is the temperature, n is the kinetic order of the desorption. A kinetic order of 0 is attributed to desorption of a multilayer of an adsorbate, a kinetic order of 1 is attributed to direct desorption of a molecular species, and a kinetic order of 2 is attributed to a multi-step desorption process (*e.g.*, recombination of atomic oxygen before desorption as molecular oxygen)³¹. The product, $v_n \times e^{-\left(\frac{E_a}{RT}\right)}$, is known as the Arrhenius equation, which gives the dependence of the desorption rate on the temperature for a chemical reaction. By using a computer controlled feedback loop, the temperature of the surface is heated at a linear rate

$$T = T_o + \beta t, \quad [3-9]$$

where T is the instantaneous temperature, T_o is the initial temperature, β is the heating rate ($^{\circ}\text{C/s}$), and t is the time in seconds. The surface coverage is temperature dependent

$$\theta = \theta(T) \quad [3-10]$$

such that an instantaneous surface coverage change with temperature is defined by

$$\frac{d\theta}{dT} = \frac{d\theta}{dt} \times \frac{dt}{dT} = \frac{d\theta}{dt} \times \frac{1}{\beta}. \quad [3-11]$$

Substituting expression [3-8] into expression [3-11] yields

$$\frac{d\theta}{dT} = \frac{1}{\beta} \times v_n \times e^{\left(\frac{-E_a}{RT}\right)} \times \theta^n. \quad [3-12]$$

The temperature at which the maximum of the pressure vs. time curve occurs can be found by taking the derivative of the change in adsorbate coverage with respect to temperature and setting this expression to zero³³

$$\left. \frac{d}{dT} \left(\frac{d\theta}{dT} \right) \right|_{T_{peak}} = -\frac{v_n \theta^n}{\beta} \frac{E_a}{RT_{peak}^2} e^{\frac{-E_a}{RT_{peak}}} + \frac{v_n n \theta^{n-1}}{\beta} \frac{d\theta}{dT} e^{\frac{-E_a}{RT_{peak}}} = 0. \quad [3-13]$$

This results in

$$n\theta^{n-1} \frac{v}{\beta} e^{-\frac{E_a}{RT_{peak}}} = -\frac{E_a}{RT_{peak}^2} \quad [3-14]$$

by substituting expression [3-12] into [3-13] and cancelling like terms. This can be rewritten as

$$\ln\left(\frac{T_{peak}^2}{\beta}\right) = \frac{E_a}{R} \frac{1}{T_{peak}} + \ln\left(\frac{E_a}{Rn\theta^{n-1}v_n}\right) \quad [3-15]$$

For first order kinetics ($n = 1$), which is expected for CO desorption from the $\text{Cr}_2\text{O}_3(0001)\backslash\text{Cr}(110)$ crystal surface, the intercept of expression [3-8] no longer depends on the coverage. By plotting $\ln\left(\frac{T_{peak}^2}{\beta}\right)$ versus $\left(\frac{1}{T_{peak}}\right)$ for various heating rates, the slope of the curve can be determined. The activation energy can be determined by taking the product of the slope and the gas constant R .

CHAPTER IV

EXPERIMENTAL RESULTS

A. PREPARATION OF THE Cr(110) SURFACE

The experiments were conducted in an UHV environment with a base pressure of approximately 4×10^{-11} Torr. Before any sample preparation was performed, the TSP was flashed for 1.5 min at 45 A. To clean the crystal surface, it was sputtered with argon ions followed by annealing to heal the surface. Since the chromium crystal had a large amount of carbon and nitrogen impurities in the bulk, several sputter/anneal cycles were needed to obtain a clean Cr(110) surface. Prior to the measurements performed in this study, the crystal had been through approximately a month of daily sputter-anneal cycles, but the bare Cr(110) surface still showed streaks and spots associated with carbon and nitrogen overlayer structures. The first two sputter/anneal cycles done for this study were performed at room temperature. To enhance the removal of bulk impurities, proceeding sputter/anneal cycles were conducted at a temperature of approximately 773 K.

The sputtering process consisted of first introducing argon gas into the chamber up to a pressure of approximately 5×10^{-5} Torr with both the turbo pump and ion pump gate valves closed. A photo of the UHV system is shown in Figure 4-1. For hot sputtering, the sample filament was then connected to a current source which was ramped to 2.5 A via a LABView program. The ion gun acceleration voltage was set to 1000 V

and the ion gun filament current to 2.2 A. The current from the sample to ground was monitored during the sputter cycle and was typically about 8 μA . The duration of each sputter cycle was 40 minutes, and the maximum temperature during the sputter cycle ranged between 283 K and 818 K.

Before performing the high temperature anneals, the gate valve to the turbo pump was first opened and then the gate valve to the ion pump was opened once the chamber pressure fell below 5×10^{-9} Torr, (see Figures 3-1a and 3-3). Electron-beam (e-beam) heating was used to perform the high temperature anneals. This was done by setting the filament current to 2.45 A and biasing the crystal at +750 V, which extracts electrons from the heater filament. The current from the high voltage power supply (emission current) was monitored using a multimeter and was typically about 5 mA. The sample was annealed for five minutes at a temperature of 993 K. The sample was allowed to cool to room temperature before another sputter/anneal cycle was conducted.

The cleanliness of the crystal surface was determined from the images observed from LEED analysis. For a clean crystal, sharp bright spots with no streaks and low diffuse background should be observed.^{1,26} As mentioned previously, new chromium single crystals typically have large amounts of nitrogen and carbon impurities. The first studies of the Cr(110) crystal were performed in a previous study.¹² A LEED image after the first 10 days of sputter-anneal cycles performed in the aforementioned study is shown in Figure 4-1a. Streaks and extra spots can be seen in this image, which are due to the segregation of carbon and nitrogen impurities to the surface. To prepare a clean surface for the growth of the epitaxial oxide, the first few weeks of my study involved the daily or sometimes twice daily sputtering and annealing of the Cr(110) crystal. LEED analyses

were conducted after the second through fifth, tenth and eighteenth sputter/anneal cycles. The analysis performed before the oxidation of the surface still revealed some streaks and extra spots in the LEED pattern, as shown in Figure 4-1b. Notably, approximately one more month of sputter/anneal cycles were performed in a study³⁷ that followed the completion of this research project. The extra month of sputter/anneal cycles resulted in the formation of a clean Cr(110) surface without any extra spots or streaks associated with C or N segregation, as seen in Figure 4-1c.

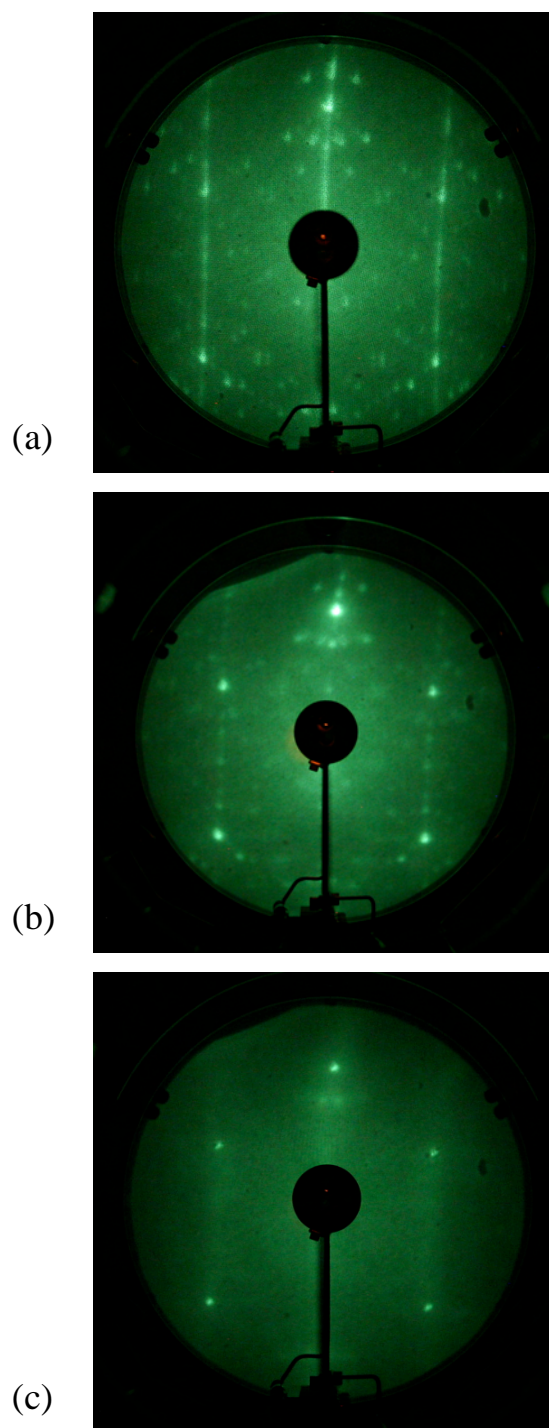


Figure 4-1 LEED analysis of Cr(110) after several sputter/anneal cycles at room temperature. The LEED images were recorded at an electron beam energy of 75 eV after (a) 12 of 15 sputter/anneal cycles performed in a previous study¹². (b) after 17 of 19 sputter/anneal cycles in my study and (c) after 2 of 36 sputter/anneal cycles performed in a study³⁷ immediately following my research project.

B. GROWTH OF EPITAXIAL $\text{Cr}_2\text{O}_3(0001)$ ON $\text{Cr}(110)$

Exposing the chromium surface to oxygen at elevated temperatures will remove any carbon at the surface by the formation of CO and CO_2 and will also displace any surface nitrogen since the binding affinity of oxygen with chromium is greater than that of nitrogen with chromium. Therefore, the formation of the epitaxial $\text{Cr}_2\text{O}_3(0001)$ surface was performed even though all of the carbon and nitrogen impurities had not been removed from the $\text{Cr}(110)$ surface. To form the oxide, the ion pump gate valve was closed, and the turbo pump gate valve was left open while oxygen was progressively introduced to backfill the chamber to a pressure of approximately 1×10^{-6} Torr. The filament current was then ramped to 2.2 A to quickly raise the temperature to 550 K. Once a temperature of 550 K was obtained, the filament current was reduced to 2.0 A to maintain the crystal at a temperature of 550 K for 1 minute. The filament current was then increased to 2.6 A to increase the temperature to 775 K. The filament current was then reduced to 2.5 A for 2 minutes to maintain the crystal at 775 K. The oxygen leak valve was then shut off, and the crystal was flashed to approximately 1000 K in UHV using e-beam heating. LEED analysis was then conducted to confirm presence of a well-ordered $\text{Cr}_2\text{O}_3(0001)$ surface structure, as shown below in Figure 4-2. Even though the LEED pattern of the $\text{Cr}(110)$ surface before oxidation did exhibit some streaks, no streaks or extra spots were observed for the LEED pattern of the $\text{Cr}_2\text{O}_3(0001)$ surface.

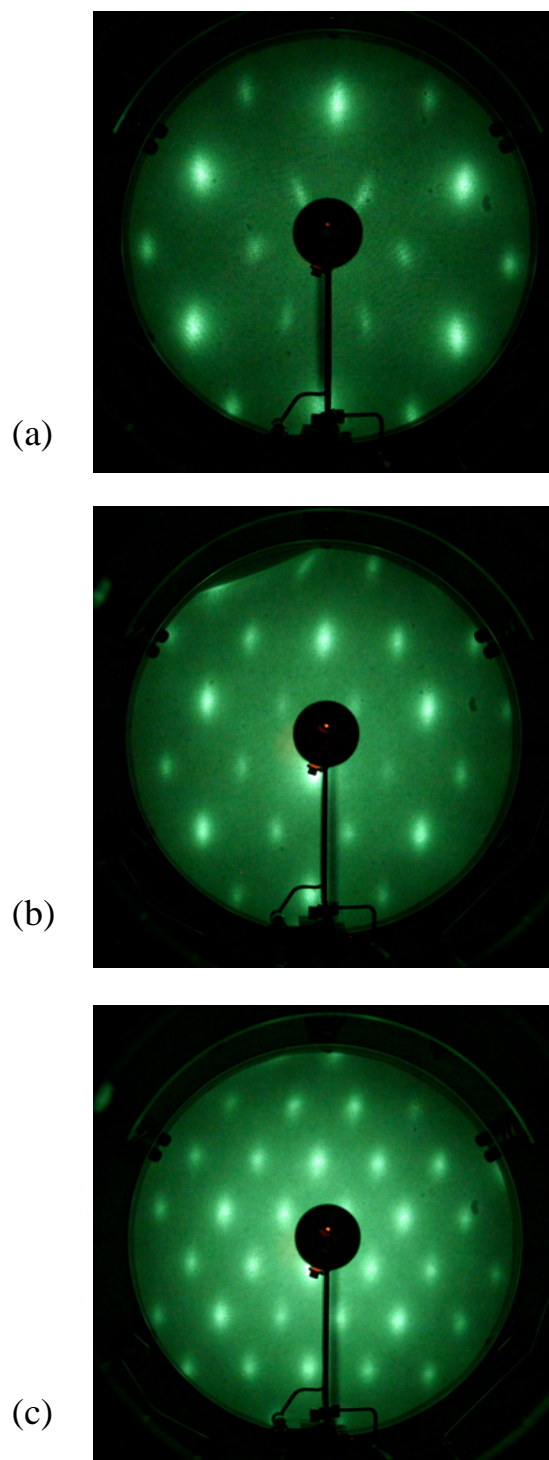


Figure 4-2: LEED analysis of $\text{Cr}_2\text{O}_3(0001)/\text{Cr}(110)$ at room temperature for this study. The images were recorded with an electron beam energy of (a) 54.5 eV, (b) 75.0 eV and (c) 112.8 eV.

C. TEMPERATURE DEPENDENT LEED ANALYSES OF $\text{Cr}_2\text{O}_3(0001)/\text{Cr}(110)$

The temperature dependence of the $\text{Cr}_2\text{O}_3(0001)/\text{Cr}(110)$ surface was previously studied by another group.¹ They observed a diffuse $(\sqrt{3}\times\sqrt{3})\text{R}30^\circ$ superstructure at room temperature that became more pronounced at 150 K and vanished between 90 K and 100 K, as shown in Figure 4-3. This transition was attributed to the antiferromagnetic coupling of the surface chromium ions. As mentioned earlier, a previous study¹² repeated these temperature dependent LEED measurements with the crystal used in this

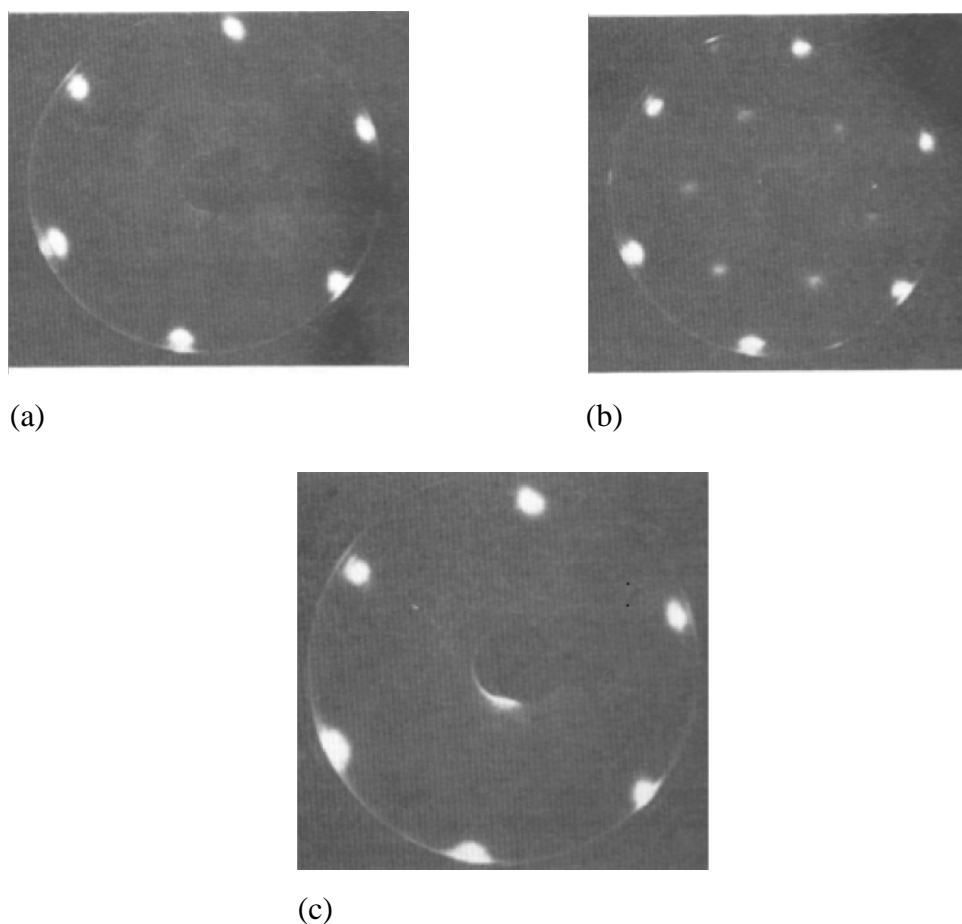


Figure 4-3: LEED analysis of $\text{Cr}_2\text{O}_3(0001)/\text{Cr}(110)$ at 300 K, 150 K and 90 K from a previous study. The images were recorded with an electron beam energy of 24 eV with a $\sqrt{3}\times\sqrt{3}\text{R}30^\circ$ reconstruction surrounding the (0,0) diffraction spot that is (a) diffuse at 300 K, (b) most pronounced at 150 K and (c) not present at 90 K. From ref. [1].

study and found no $(\sqrt{3}\times\sqrt{3})R30^\circ$ superstructure over a temperature range of 140 K to 675 K. Since it is possible that nitrogen and carbon impurities in the near surface region might have affected the Cr_2O_3 overlayer structure, these temperature dependent LEED measurements were repeated on a cleaner Cr(110) substrate as part of this research project. LEED measurements of the $\text{Cr}_2\text{O}_3(0001)/\text{Cr}(110)$ surface were performed at room temperature and at approximately 120 K as shown in Figure 4-4. No evidence of a $(\sqrt{3}\times\sqrt{3})R30^\circ$ surface structure reconstruction was observed.

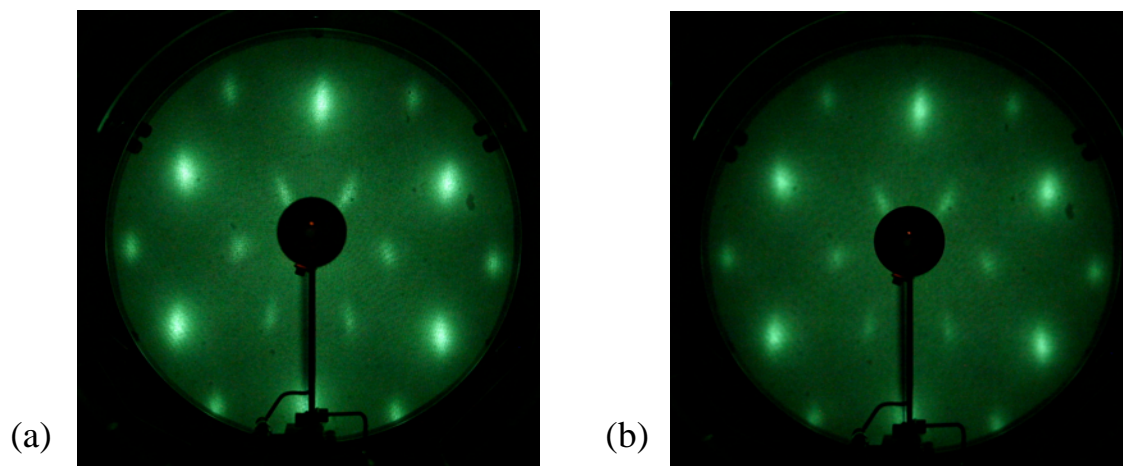


Figure 4-4: LEED analysis of $\text{Cr}_2\text{O}_3(0001)/\text{Cr}(110)$ at ~ 300 K and 125 K for this study. The images were recorded with an electron beam energy of 54.5 eV for temperatures of (a) ~ 300 K and (b) 125 K.

D. ADSORPTION OF CARBON MONOXIDE ON Cr₂O₃(0001)/Cr(110)

i. CO Dosing Sequence

Before dosing the crystal with CO, it was flashed for 1 minute at 750 K and allowed to cool to room temperature before being cooled using liquid nitrogen. The liquid nitrogen-cooling process took up to one hour to approach typical temperatures between 140 K and 122 K. The cooling process was necessary since CO does not stick on the Cr₂O₃(0001) surface at room temperature. Carbon monoxide was then supplied to the vacuum chamber through a variable leak valve that was connected to a CO lecture bottle. A CO dosing sequence was performed to determine the saturation dosage for the Cr₂O₃(0001) surface. In Figure 4-5 the TPD spectra for dosages of 0.1 L, 0.2 L, 0.3 L, 0.5 L, 10 L, and 20 L can be seen, where 1 Langmuir (L) is defined as 1×10^{-6} Torr·s. For these measurements, the linear translator of the mass spectrometer was set at 42 mm each time, which results in the collimator of the mass spectrometer being within a couple of millimeters of the surface of the crystal. The parameters of the TPD measurements were a heating rate of 10 °C/min, an initial current of 0.5 A, a feedback constant of .0015, a final current of 3.5 A, a shut off temperature of 475 K, and a time delay of 1000 ms. To determine the relative coverages associated with each dosage, the areas under the pressure versus time curves were calculated. A compilation of these relative coverages is given in Table 4-1. As can be seen in the table, the saturation coverage is achieved at approximately 0.5 L.

A previous study² reported that the saturation coverage of CO on the Cr₂O₃(0001) surface exhibits a $(\sqrt{3} \times \sqrt{3})R30^\circ$ symmetry. However, this pattern was only observed within the first 10 s after the introduction of CO, which indicates that the CO is

easily desorbed by low energy electron interactions. The LEED images of the CO covered surface after dosing 1L and 10L at 147 K are shown in Figure 4-6. These images were taken after a few minutes of exposure to the electron beam. As with the previous measurements,² no overlayer reconstruction is observed, which is expected if the CO is sensitive to electron beam desorption.

The TPD spectra represented in Figure 4-5 also show an overall shift of 4 K in the temperature of the TPD peak from initial coverage to saturation, as noted in Table 4-2. The slight shift in peak desorption temperatures indicates that CO desorbs from the Cr₂O₃(0001)/Cr(110) surface as a 1st order kinetics, which has been found in previous studies. This indicates that the CO molecules adsorb molecularly (i.e., they do not dissociate upon adsorption). The slight increase in the temperature of the desorption peak with coverage probably results from an attractive CO-CO interaction.

It is important to understand that area under the pressure versus temperature graphs do not represent the adsorbate surface coverage. To extract information regarding the adsorbate surface coverage, it is necessary to compute and analyze the areas under the pressure versus time curves. For this study, analysis of the area under the pressure versus time curves verified that CO saturated on the chrome oxide surface at approximately 0.5 L as was observed graphically and tabulated in Table 4-1.

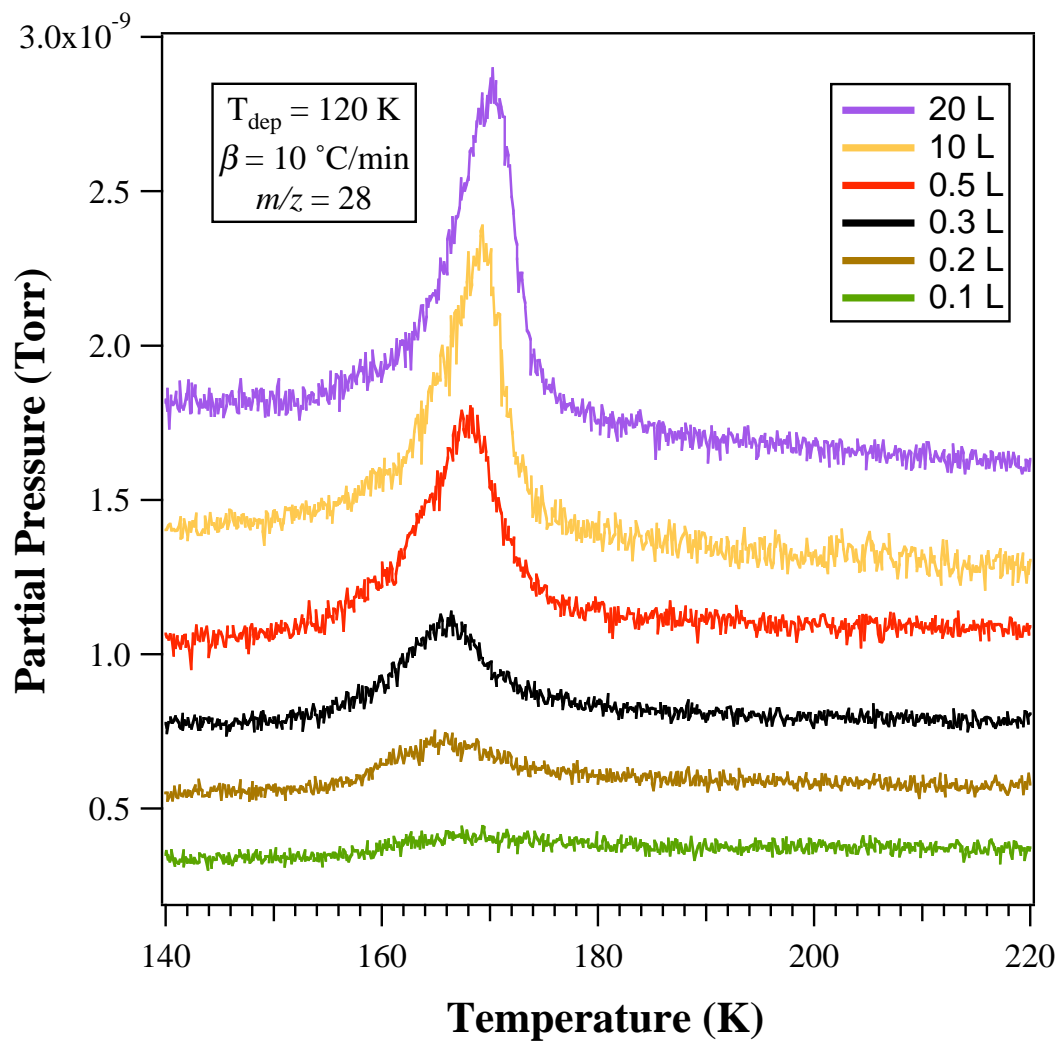


Figure 4-5: TPD spectra of CO from the $\text{Cr}_2\text{O}_3(0001)/\text{Cr}(110)$ surface at a heating rate of $10 \text{ }^\circ\text{C/min}$ for different doses of CO. TPD spectra for doses of 0.5 L, 10 L, and 20 L are similar, indicating that CO adsorption saturates at a dose of $\sim 0.5\text{L}$. The slight shift in the temperature of the TPD peak indicates that CO desorbs as a 1st order kinetics.

NOTE: The ordinate of the pressure vs. temperature graph is offset in order to better resolve the TPD spectra at the different doses.

Table 4-1: Areas calculated from pressure versus time curve and corresponding temperature of the maximum of the TPD peak. A CO dose of 1 L was used in this study to ensure that a saturation layer of CO was adsorbed on the

Temperature Programmed Desorption of CO from Cr ₂ O ₃ (0001)/Cr(110) Area under the Pressure versus Time curve		
CO Dose (L)	Area (Torr*s)	Peak Temperature (K)
0.1	1.30×10^{-8}	
0.2	2.65×10^{-8}	166
0.3	3.28×10^{-8}	166
0.5	6.26×10^{-8}	168
10	6.41×10^{-8}	169
20	6.57×10^{-8}	170

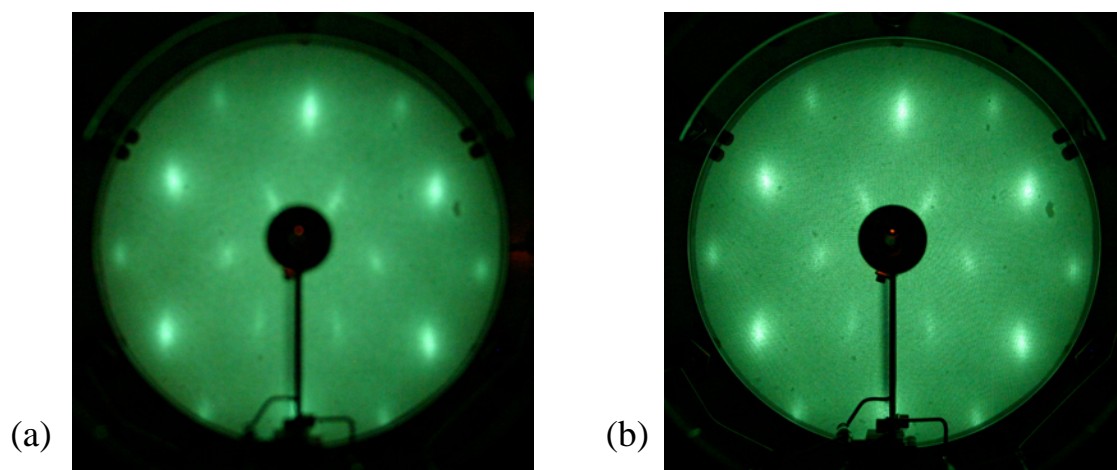


Figure 4-6: LEED analysis of CO/Cr₂O₃(0001)/Cr(110) for doses of 1 L and 10 L. The analysis was conducted at 147 K with an electron beam energy of 55 eV and a CO dose of (a) 1 L and (b) 10 L.

ii. Dependence of TPD Spectra on Heating Rate

For a fixed CO coverage, the temperature at which the peak desorption pressure occurs depends on the heating rate. An example of this is shown in Figure 4-7 for 1 L CO on Cr₂O₃(0001)/Cr(110) with heating rates of 5, 10, 25, and 50 °C/min. The desorption rate, $d\theta/dT$, depends on the surface coverage θ and the Boltzmann factor, as

defined by $\frac{d\theta}{dT} = \frac{1}{\beta} \times v_n \times e^{\left(\frac{-E_a}{RT}\right)} \times \theta^n$ (equation 3-12). As the temperature increases, the

probability of desorption increases, resulting in a decrease in the surface coverage. Since there is a finite amount of adsorbate on the surface, increasing the temperature will eventually result in a change from an increasing desorption rate to a decreasing desorption rate, resulting in a peak in the TPD curve. For higher heating rates, the TPD peak will shift to higher temperatures than for lower heating rates, as shown in Figure 4-7. The reason for this is that the desorption probability increases with temperature, so a fast heating rate results in less time at a particular temperature for the adsorbate atoms to desorb.

In this study, the crystal surface was cooled to within 120 K, then a saturation layer of 1 L of CO was dosed onto surface as described in section (i) above. To achieve a 1 L dose of CO, it was introduced via a leak valve at a background pressure of 5×10^{-9} Torr for 200 seconds with the gate valve to the ion pump closed. After 200 seconds the CO leak valve was shut and the gate valve to the ion pump was opened to the chamber after a pressure in the 1×10^{-10} Torr was obtained. The chamber was then monitored using the QMS, prior to heating the sample, to verify pressure stability of the chamber with respect to any degassing particles. Once it was determined that the chamber

environment was stable, TPD analysis was performed for various heating rates. TPD analysis for heating rates of 5 °C/min, 10 °C/min, 25 °C/min and 50 °C/min were performed on two separate days. During the TPD analysis, the gate valve to the turbo pump and the gate valve to the ion pump were left open to ensure that the registered CO desorption pressure at the mass spectrometer was proportional to the rate of desorption from the crystal surface. The temperature of the TPD peak maximum, as observed in the pressure versus temperature graph for CO desorption from the Cr₂O₃(0001)/Cr(110) surface, increases with increasing heating rate. The areas under the pressure-time curves and the corresponding peak maxima temperatures of desorption for each heating rate is presented in Table 4.2. For a saturation coverage of CO, the area under the pressure-time curve should be independent of heating rate. As seen in Table 4-2, there is only a 6% difference between the lowest and highest area.

The values for the areas under the pressure-time curves listed in Table 4-1 are about 20% larger than those listed in Table 4-2. This most likely is the result of a difference in the position of the mass spectrometer during the measurements. For the first series of measurements, the position of the linear translator was determined by reading directly off of its scale. For subsequent measurements, a ruler along with the scale markings on the linear translator were used to determine the position of the mass spectrometer, which probably caused a change in its absolute position.

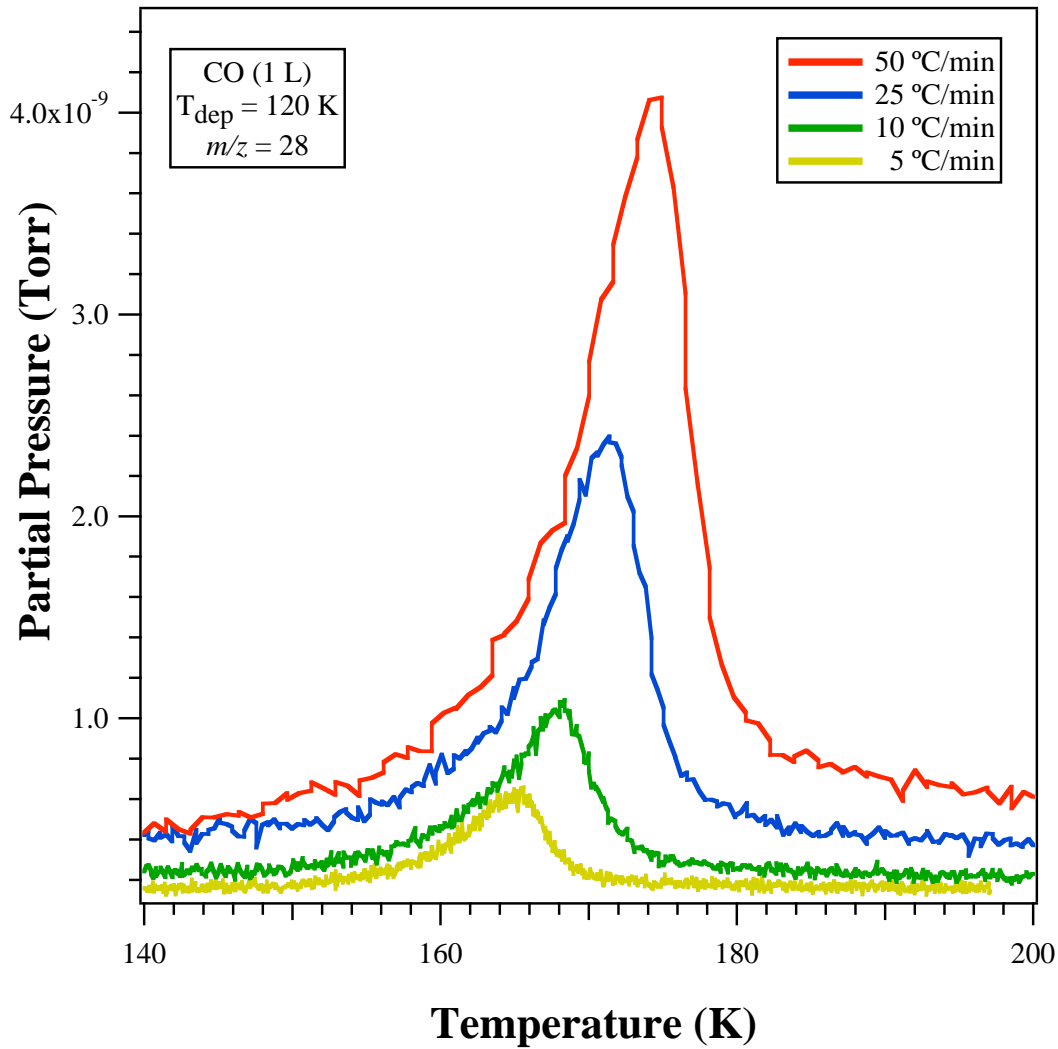


Figure 4-7: Pressure versus temperature curves for several heating rates for a CO dose of 1.0 L. The inset shows a temperature versus time graph for the heating rate of 10°C/min.

Table 4-2: Areas calculated from pressure versus time curve and the temperature of the maximum of the TPD peak for heating rates ranging from 5 °C/min to 50 °C/min for a dose of 1.0 L of CO. Pressure versus temperature curves are shown in Figure 4-7.

Temperature Programmed Desorption of CO from Cr ₂ O ₃ (0001)/CO(110) Average Desorption Peak Temperature		
Heating Rates (°C/min)	Area (Torr*s)	Peak Temperature (K)
5	4.9 x 10 ⁻⁸	165
10	5.0 x 10 ⁻⁸	168
25	4.7 x 10 ⁻⁸	171
50	4.7 x 10 ⁻⁸	174

iii. Activation Energy Analysis

CO desorption from the Cr₂O₃(0001)/Cr(110) surface, for a linear heating rate, was found to desorb as a first order kinetics. Employing the Redhead method, which is valid for a first order desorption, $n = 1$, and a linear heating rate, $\beta = \frac{\partial T}{\partial t} = \text{constant}$, a coverage independent expression is found that relates the activation energy, E_a , to the temperature of the desorption rate maximum, T_{peak} , and to the heating rate, β . The

activation energy is calculated from the slope of the graph of the $\ln\left(\frac{T_{\text{peak}}^2}{\beta}\right)$ versus

$\left(\frac{1}{T_{\text{peak}}}\right)$ for various heating rates. For this study, heating rates of 5 °C/min, 10 °C/min,

25 °C/min and 50 °C/min were used. Three runs were performed with each heating rate except 10 °C/min, where two measurements were made. The temperatures, T_{peak} , and

corresponding heating rates that are listed in Table 4-3, were plotted and a linear regression line was fit to the points as shown in Figure 4-8. The value of the slope of the equation of the linear regression resulted in an activation energy of 49.2 ± 2.6 kJ/mol.

Table 4-3: Temperature of the maximum of the TPD peak for each dose of 1.0 L of CO.

Heating Rate, β (°C/min)	T_{peak} (K)		
5	164	168	168
10	165	168	*
25	171	172	171
50	175	177	174

**Data lost due to software failure*

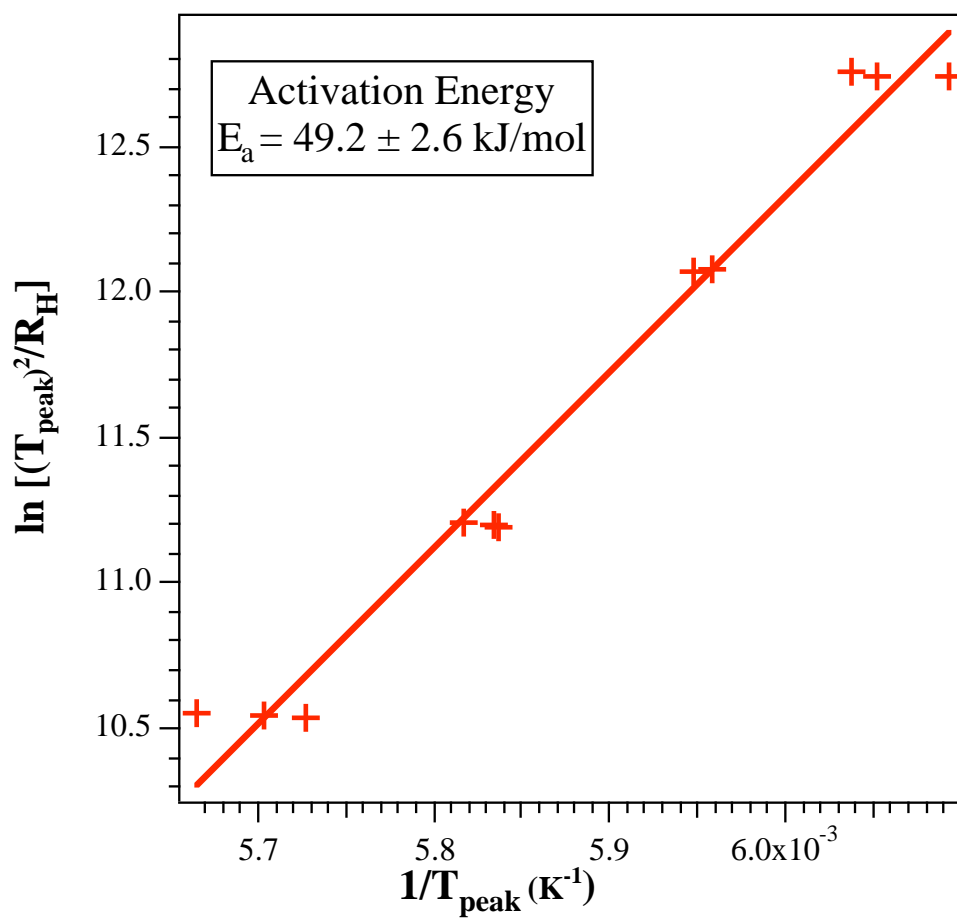


Figure 4-8: Arrhenius plot assuming first order desorption kinetics for a dose of 1.0 L of CO. The product of the slope of the linear fit line and the gas constant, R , yields a value for the activation energy, E_a , for desorption.

CHAPTER V

DISCUSSION

The presence of extra spots in the LEED pattern of the Cr(110) surface during the first several months of cleaning the crystal with sputter/anneal cycles provides evidence that bulk impurities (most likely nitrogen and carbon) were diffusing to the surface during the annealing process. Even though the Cr(110) surface had some impurities, the growth of the oxide resulted in a well-ordered surface structure of Cr₂O₃(0001)/Cr(110) as observed in the LEED analysis. This provides evidence that exposure to oxygen helped clean the surface of the nitrogen and carbon impurities.

LEED analyses of the Cr₂O₃(0001)/Cr(110) surface at temperatures as low as 120 K failed to reveal the presence of a ($\sqrt{3}\times\sqrt{3}$) R30° superstructure as discussed in a previous study.¹ The absence of the superstructure in our studies could be attributed to the lower base pressure of the chamber. The base pressure of the chamber in our studies was 4×10^{-11} Torr, while the base pressure in the Bender study was 2×10^{-10} Torr. It could be that for the measurements of Bender et al. gas molecules in the chamber were adsorbing on the surface as the temperature was reduced below 150 K, resulting in an ordered overlayer of adsorbates. Since CO adsorption on the Cr₂O₃(0001)/Cr(110) surface has been observed to give rise to a ($\sqrt{3}\times\sqrt{3}$) R30° superstructure,² the superstructure observed in a different study¹ could have been from CO adsorption from the residual gas in the chamber. In addition, CO₂, which is also present as a residual gas

in UHV, could possibly have adsorbed on the surface, producing an overlayer structure. The disappearance of the $(\sqrt{3}\times\sqrt{3})$ R30° superstructure below 100 K as observed by another group¹ could have resulted from multilayer adsorption of CO₂ since this occurs at about 90 K.

Another factor that must be considered in possibly explaining the lack of a $(\sqrt{3}\times\sqrt{3})$ R30° superstructure is that the tolerance of the alignment of the Cr(110) crystal surface used in our study was more precise than the tolerance of the crystal surface in a previous study.¹ The Cr(110) crystal in our study was oriented to within $\pm 0.1^\circ$ from the [110] direction, the crystal used in the previous study¹ was oriented to within $\pm 0.5^\circ$ from the [110] direction. The tolerance in the orientation of the (110) surface for our study produces a terrace length that is five times greater than the terrace length for the crystal used by another research group.¹ Since strain in the overlayer is relieved at step edges, the oxide films grown on a misaligned crystal will have smaller terraces and thus less residual strain within the film. This might also have led to geometrical differences between the Cr₂O₃(0001)/Cr(110) surface of the crystal used in my study and the surface of the crystal used in a similar study.¹

Temperature programmed desorption measurements of CO from the Cr₂O₃(0001)/Cr(110) surface at heating rates of 5, 10, 25 and 50 °C/min were conducted. The TPD measurements were conducted with the mass spectrometer positioned within a few millimeters of the crystal surface and within ± 0.5 mm of the same location for each measurement. The adsorption temperatures were always between 120 K and 140 K. Temperatures below 120 K were not attainable due the limited heat transfer rate from the crystal to the Dewar. This limitation was primarily caused by using tantalum wires,

which are poor thermal conductors, to mount the crystal to the molybdenum insert. To lower the temperature further, tungsten wires should be used instead. However, it is much more difficult to spot weld tungsten to either chromium or molybdenum. The capability to drop below temperatures of 120 K would have allowed for further investigation of the adsorption of CO just beyond the first monolayer on the $\text{Cr}_2\text{O}_3(0001)/\text{Cr}(110)$ surface as it has been done in other studies including the one by Bender et al. To achieve true multilayer adsorption, a liquid He dewar would be needed since previous studies have shown that the multilayer desorbs near 30 K.

The TPD data are currently taken using two separate programs, run simultaneously. The one program creates the linear temperature ramp and collects the temperature and time signature. The second program measures the partial pressures of up to 8 different gases and also collects the time signature. A linear time dependent temperature equation was calculated to match each temperature datum to each pressure datum with respect to the time the datum that was stored. The reason that two programs are run simultaneously is to prevent conflicts with trying to read/write to the Hiden controller and the NI data acquisition board within the same LabView program. If a method for performing both duties within that same program could be found, this would simplify the data analysis.

One of the main goals of this research project was to accurately measure the activation energy for CO desorption from the $\text{Cr}_2\text{O}_3(0001)/\text{Cr}(110)$ surface. A previous study had predicted a value of 28 kJ/mol using cluster calculation; whereas, they had estimated an activation energy of 45 kJ/mol using TPD. My measurements result in a value of 49.2 ± 2.6 kJ/mol. In addition, my uptake measurements are consistent with a

first order desorption kinetics. Therefore, it is clear that the cluster calculations are underestimating the activation energy for desorption by about a factor of two.

CHAPTER VI

CONCLUSIONS

It was determined that the chromium crystal, Cr(110), needed several months of sputtering and annealing cycles to remove enough of the bulk impurities to result in a surface with minimal streaking in the LEED pattern. Although all of the extra LEED spots from impurity atoms on the Cr(110) surface were not removed during this measurement time, oxidation of the surface was found to result in a well ordered Cr₂O₃(0001)/Cr(110) surface. This was evidenced by the hexagonal LEED pattern with low diffuse background, which meant that a well structured Cr₂O₃(0001) surface was successfully grown on the Cr(110) surface.

LEED analyses of the Cr₂O₃(0001)/Cr(110) surface at room temperature and at temperatures as low as 120 K did not show a temperature dependent ($\sqrt{3}\times\sqrt{3}$) R30° surface reconstruction, as was observed by previous groups.^{1,2} The most likely reason for this result is either the better base pressure of our UHV chamber or differences in the residual strain in the Cr₂O₃(0001) film from a better surface alignment.

TPD measurements were performed with increasing CO dosages on the Cr₂O₃(0001)/Cr(110) surface, and it was determined that a saturation of CO was achieved for a dose of approximately 0.5 L. The slight shift in the temperature of the TPD peak to higher temperature as the CO dose was increased, provides evidence for a 1st order desorption kinetics with an attractive adsorbate-adsorbate interaction. By applying the

Redhead method for a first order desorption kinetics, an activation energy of 49.2 ± 2.6 kJ/mol was determined. This value agrees well with a value of 45 kJ/mol found in a previous study.²⁰

References

1. M. Bender, D. Ehrlich, I. N. Yekovkin, F. Rhor, M. Bäuer. H. Kuhlenbeck, H.-J. Freund, and V. Staemmler, *Structural Rearrangement and Surface Magnetism on Oxide Surfaces: A Temperature- Dependent Low-Energy Electron Diffraction- Electron Energy Loss Spectroscopy Study of Cr₂O₃(111)/Cr(110)*, J. Phys.: Condens. Matter **7**, 5289 (1995).
2. C. Xu, B. Dillman, H. Kuhlenbeck, and H.-J. Freund, *Unusual State of Adsorbed CO: CO($\sqrt{3}\times\sqrt{3}$)R30°/Cr₂O₃(111)*, Phys. Rev. Lett. **67**, 3551 (1991).
3. F. Rohr, M. Bäumer, H. -J. Freund, J. A. Mejias, V. Staemmler, S. Müller, L. Hammer and K. Heinz, *Strong relaxations at the Cr₂O₃(0001) surface as determined via low-energy electron diffraction and molecular dynamics simulations*, Surf. Sci. **372**, L291 (1997).
4. A. J. Rowley, M. Wilson and P. A. Madden, *Crystal structure and surface relaxation in with a transferable oxide interaction potential*, J. Phys.: Condens. Matter **11**, 8 (1999).
5. C. Rehbein , N. M. Harrison, A. Wander, *Structure of the α -Cr₂O₃ (0001) surface: An ab initio total-energy study*, Phys. Rev. B **54**, 14066 (1996).
6. X.-G. Wang and J. R. Smith, *Surface phase diagram for Cr₂O₃(0001): Ab initio density functional study*, Phys. Rev. B **68**, 201402 (2003).
7. A. Rohrbach, J. Hafner, and G. Kresse, *Ab initio study of the (0001) surfaces of hematite and chromia: Influence of strong electronic correlations*, Phys. Rev. B **70**, 125426 (2004).
8. Maike Lübbe and Wolfgang Moritz, *A LEED analysis of the clean surfaces of α -Fe₂O₃(0001) and α -Cr₂O₃(0001) bulk single crystals*, J. Phys.: Condens. Matter **21**, 134010 (2009).
9. K. Wolter, D. Scarano, J. Fritsch, H. Kuhlenbeck, A. Zecchina and H. -J. Freund, *Observation of a localized surface phonon on an oxide surface*, Chem. Phys. Lett. **320**, 206 (2000).
10. T. Gloege, H. L. Meyerheim, W. Moritz and D. Wolf, *X-ray structure analysis of the Cr₂O₃(0001)-(1×1) surface: evidence for Cr interstitial*, Surf. Sci. Lett. **441**, L917 (1999).

11. E. J. Samuelsen, M. T. Hutchings and G. Shirane, *Inelastic neutron scattering investigation of spin waves and magnetic interactions in Cr₂O₃*, *Physica* **48**, 13 (1970).
12. S. Redding, *Low Energy Electron Diffraction Study of Epitaxial Cr₂O₃(0001) Films Grown on Cr(110)* (University Honors Thesis, Texas State University–San Marcos, TX 2009).
13. H. Kuhlenbeck, C. Xu, B. Dillman, M. Habel, B. Adam, D. Ehrlich, S. Wohlrab, H.-J. Freund, U. A. Ditzinger, H. Neddermeyer, M. Neuber, and M. Neumann, *Adsorption and reaction on oxide surfaces: carbon monoxide and carbon dioxide on chromium oxide (Cr₂O₃)(111)*, *Phys. Chem.* **96**, 15 (1992).
14. M. I. Zaki and H. Knözinger, *An infrared spectroscopy study of carbon monoxide adsorption on α -chromia surfaces: Probing oxidation states of coordinatively unsaturated surface cations*, *J. Catal.* **119**, 2 (1989).
15. D. Scarano and A. Zecchina, *Adsorbate-adsorbent and adsorbate-adsorbate interactions in CO overlayers adsorbed on α -Cr₂O₃ as investigated by infrared spectroscopy*, *Spectrochim. Acta* **43A**, 12 (1987).
16. D. Scarano, A. Zecchina, and A. Reller, *IR study of CO adsorption on α -Cr₂O₃*, *Surf. Sci.* **198**, 11 (1988).
17. D. Scarano, G. Spoto, S. Bordiga, G. Ricchiardi and A. Zecchina, *Revisiting the α -Cr₂O₃/CO interaction: an FTIR and HRTEM study*, *J. Electron. Spectrosc. Relat. Phenom.* **64/65**, 307 (1993).
18. A. Zecchina, D. Scarano, S. Bordiga, G. Ricchiardi, G. Spoto and F. Geobaldo, *IR studies of CO and NO adsorbed on well characterized oxide single microcrystals*, *Catal. Today* **27**, 403 (1996).
19. I. Beauport, K. Al-Shamery and H.-J. Freund, *Rotational alignment in the UV-laser induced desorption of CO from Cr₂O₃(0001)*, *Chem. Phys. Lett.* **256**, 6 (1996).
20. M. Pykavy, V. Staemmler, O. Seiferth, H.-J. Freund, *Adsorption of CO on Cr₂O₃(0001)*, *Appl. Surf. Sci.* **253**, 7108 (2007).
21. P. S. Robert, H. Geisler, C. A. Ventrice, J. van Ek, S. Chaturvedi, J. A. Rodriguez, M. Kuhn, and U. Diebold, *Novel Electronic and Magnetic Properties of Ultrathin Chromium Oxide Films Grown on Pt (111)*, *J. Vac. Sci. Technol. A* **16(3)**, 990 (1998).
22. S. Funk, T. Nurka, B. Hokkanen, U. Burghaus, *CO₂ Adsorption on Cr(110) and Cr₂O₃(001)/Cr(110)*, *Appl. Surf. Sci.* **253**, 7108 (2007).

23. D. P. Mann, T. Paraskeva, K. F. E. Pratt, I. P. Parkin, and D. E. Williams, *Metal Oxide Semiconductor Gas sensors Utilizing a Cr-Zeolite Catalytic Layer for Improved Selectivity*, Meas. Sci. Technol. **16**, 1193 (2005).
24. Charles Kittel, *Introduction to Solid State Physics*, 8th Ed. (John Wiley and Sons, Inc., Hoboken, NJ 2005), pp. 4, 15, 25-32, 489, 491.
25. G. Ertl and J. Küppers, *Low Energy Electrons and Surface Chemistry*, (Verlag Chemie, Weinheim 1974), pp. 1-10, 129-144.
26. A. W. Hull, *X-Ray Crystal Analysis of Thirteen Common Metals*, Phys. Rev. **17**, 571 (1921).
27. R. W. G Wyckoff, *Crystal Structures: Inorganic Compounds RX_n , R_nMX_2 , R_nMX_3* , 2nd Ed., Volume 2, (John Wiley and Sons, Inc., New York, NY 1964), pp. 6-8.
28. M. A. Omar, *Elementary Solid State Physics*, (Addison-Wesley, London 1975), pp.37-46.
29. J. R. Christman, *Fundamentals of Solid State Physics*, (Wiley, New York, NY 1988), pp. 75-85.
30. R. L Park, (1985). *Methods of Experimental Physics-Solid State Physics: Surfaces* , Vol. 22 (Academic Press, Inc., Orlando, FL 1985), pp.425-464.
31. P. A. Redhead, *Chemisorption on Polycrystalline Tungsten. Part 1. – Carbon Monoxide*, Trans. Faraday Soc. **57**, 641 (1961).
32. N. Clark, (2009). *Design of a Temperature Programmed Desorption System for the Measurement of the Desorption Kinetics of Molecules from Surfaces* (M.S. Thesis, Texas State University-San Marcos, TX 2009).
33. M. Schmid, M. Pinczolits, W. Hebenstreit, P. Varga, *The Nitrogen-Induced Herringbone Reconstruction of Cr(110)*, Surf. Sci. **389**, L1140 (1997).
34. National Aeronautics and Space Administration, Atmospheric Experiments Laboratory, <http://ael.gsfc.nasa.gov/images/saturn/msSchematic.gif>.
35. *ITS-90 Thermocouple Direct and Inverse Polynomials. Type K Thermocouple*. <http://www.omega.com/temperature/Z/pdf/z198-201.pdf>, p. Z-196.
36. J. Walters. (2010). *Measurement of the Adsorption Kinetics of CO and CO₂ on Cr(110)* (M.S. Thesis, Texas State University-San Marcos, TX 2010).

VITA

Gabriel Arellano was born in El Paso, TX to Eduardo Arellano and Gabriela Manriquez de Arellano. He has one older brother, Miguel Hector Arellano, two older sisters, Gabriela Arellano and Rebeca Arellano, and two younger brothers, Rafael Arellano and Guadalupe Arellano.

Gabriel Arellano attended Vilas Elementary, Lamar Middle School and finally El Paso High School before beginning his collegiate career at the University of Texas at El Paso. Gabriel Arellano had an interest in architecture and transferred to the University of Texas at Austin in order to study the subject. During his early studies, Gabriel Arellano found that he had a greater interest in Physics and decided to study and major in the subject. Gabriel Arellano successfully completed his undergraduate work and earned his Bachelor of Science in Physics from the University of Texas at Austin. After a few years, Gabriel Arellano applied and was accepted to the Master of Science in Physics program at Texas State University-San Marcos. Gabriel Arellano was able to successfully complete the program in 2 years under the careful guidance of Dr. Carl A. Ventrice Jr. Gabriel Arellano currently works for Austin Community College as a Sr. Computer Lab Support Technician and as a tutor in the subjects of Physics, Mathematics and Spanish.

Gabriel Arellano enjoys swimming, running and cycling. Gabriel Arellano, who once played the violin exceptionally well and who played classical guitar not so well, expects to begin anew with guitar lessons and continue where he left off several years

